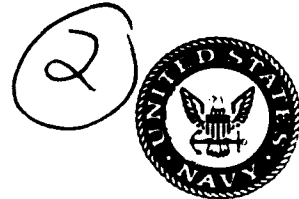


2  
COPY

# Naval Research Laboratory

Washington, DC 20375-5000



NRL Memorandum Report 6681

AD-A226 537

## NRL Compact Accelerator Theory Studies

R. F. HUBBARD, A. W. ALI, G. JOYCE, J. KRALL, F. MAKO,\*  
P. SERAFIM,\*\* S. P. SLINKER, P. SPRANGLE AND C. M. TANG

*Plasma Physics Division*

\**FM Technologies, Inc., Alexandria, VA 22304*

\*\**Northeastern University, Boston, MA 02115*

DTIC  
S ELECTE SEP 13 1990 D  
D CG

August 31, 1990



## CONTENTS

INTRODUCTION .....	1
ELBA — A THREE-DIMENSIONAL PARTICLE SIMULATION CODE .....	5
STABILITY REGIMES IN A ROTATING QUADRUPOLE FOCUSING ACCELERATOR .....	9
THREE-DIMENSIONAL SIMULATIONS OF ELECTROMAGNETICALLY STABLE AND UNSTABLE REGIMES IN THE SPIRAL LINE INDUCTION ACCELERATOR .....	13
THREE-DIMENSIONAL SIMULATIONS OF BEAM TRANSPORT AND EMITTANCE GROWTH IN THE SPIRAL LINE INDUCTION ACCELERATOR .....	17
NRL STUDIES OF RLA ACCELERATOR PHYSICS .....	21
EROSION OF ELECTRON BEAMS IN THE RLA ACCELERATOR .....	25
ATOMIC AND PLASMA SURFACE INTERACTIONS IN ACCELERATORS AND IFR CELLS .....	29
DISTRIBUTION LIST .....	33



Accumulation File	
NTIS Serial	1
DTIC TABS	1
Unnumbered	0
Justification	
By _____	
Distribution / _____	
Availability Codes	
Dist	Avail and/or Special
A-1	

## NRL COMPACT ACCELERATOR THEORY STUDIES

### INTRODUCTION

This report contains seven short papers which will appear in the Proceedings of the 1989 Annual DARPA/SDIO/Services Charged Particle Beam Review which took place at the Naval Postgraduate School in Monterey, CA during 18-21 September, 1989. The papers describe theoretical studies which support two compact accelerator experiments: the Spiral Line Induction Accelerator (SLIA) at Pulse Sciences, Inc. and the Recirculating Linear Accelerator (RLA) at Sandia National Laboratories.

Both accelerators use high current induction accelerator technology developed for the ATA and RADLAC accelerators. To reduce the weight and volume of the accelerator, the beam will be recirculated through the same accelerating cavity several times. The SLIA uses ferrite-loaded cavities similar to those used on ATA and employs stellarator coils to provide strong focusing in the curved sections of the beamline. The RLA uses dielectric cavities and relies on the electrostatic focusing of an ion channel to provide strong focusing. The NRL studies presented here include analytical and simulation modeling of beam transport and accelerator instabilities. The simulations have employed the ELBA code, a new three-dimensional particle code capable of treating both straight and curved sections of the accelerator.

A brief summary of each paper and a list of co-authors for each are provided below.

**A. ELBA - A Three-Dimensional Particle Simulation Code:** ELBA is a beam simulation code which treats particle dynamics fully-relativistically and solves Maxwell's equations using  $r$ ,  $\theta$ ,  $\zeta = ct - z$ , and  $t$  as the independent variables. The code treats propagation in curved sections of an accelerator by using a mapping technique developed by Friedman of LLNL. The code has been used to model beam transport and three-wave instability growth in the SLIA and inductive erosion and off-axis drifting in the RLA. (Joyce, Krall, Slinker)

**B. Stability Regimes in a Rotating-Quadrupole Focusing Accelerator:** The SLIA will use rotating quadrupole or stellarator fields to provide strong focusing in the curved sections of the accelerator. Beam disruption from the three-wave electromagnetic instability has been a major concern. A

linear dispersion relation has been derived for this instability assuming a thin, cold beam propagating in a cylindrical waveguide with specified solenoidal and rotating quadrupole external magnetic fields. The beam centroid may be orbit unstable, three-wave unstable or fully stable depending on the beam and external field parameters. Analytical expressions for the boundaries between these regimes have also been derived, making it possible to illustrate graphically the regions of stability and instability. The model predicts that the SLIA proof-of-concept experiment should be able to avoid the instability entirely if operated in the reversed-helicity regime suggested by Chernin and Hughes. At higher energies, it should be possible to remain in the stable regime by decreasing the quadrupole gradient in the high energy bends. These results are consistent with independent calculations by MRC and SAIC. (Tang, Sprangle, Krall, Serafim, Mako)

C. Three-Dimensional Simulations of Electromagnetically Stable and Unstable Regimes in the Spiral Line Induction Accelerator: The ELBA simulation code has been used to simulate the Three-wave instability described above. The simulations included the appropriate external fields and employed the STELMAT algorithm from SAIC for matching the beam initially. Five simulations were carried out with  $\gamma = 7$ , 7 kA beam current, 200 G/cm quadrupole gradient,  $0.5 \text{ cm}^{-1}$  quadrupole wavenumber, 3 cm wall radius, 0.158 cm-rad normalized rms emittance, and a guide field  $B_z$  from 1 to 6 kG. The linear theory described above predicts three-wave instability for  $B_z = 1, 2$  and  $4.5 \text{ kG}$ , orbit instability at  $B_z = 4 \text{ kG}$ , and stability at  $B_z = 9 \text{ kG}$ , and the individual simulations confirm those predictions. The simulation growth rates in the three-wave unstable regime were significantly lower than those predicted by the dispersion relation, however, and the source of this discrepancy is still under investigation. Stable propagation was also observed for  $B_z = -5 \text{ kG}$  and a low quadrupole gradient, but this stability regime is very narrow and thus much less useful experimentally. The results support the conclusion from the analytical models that the SLIA proof-of-concept experiment can operate entirely in the stable regime. (Krall, Tang, Joyce)

D. Three-Dimensional Simulations of Beam Transport and Emittance Growth in the Spiral Line Induction Accelerator: The ELBA code was used to model transport in an idealized transition region between purely-solenoidal and solenoidal/stellarator sections of SLIA. Emittance growth in these

transitions is a major potential problem in some parameter regimes. When a high-eccentricity equilibrium was chosen in conjunction with a long stellarator pitch length, normalized rms emittance grew by as much as 47% in a single transition. When the pitch length was shortened to a length comparable with the ramp length of the stellarator field, emittance growth was reduced substantially. The choice of a low eccentricity equilibrium resulted in negligible emittance growth, but this regime may be less desirable for other reasons. (Krall, Joyce)

**E. NRL Studies of RLA Accelerator Physics:** The Recirculating Linear Accelerator (RLA) currently under development at Sandia National Laboratories uses ion-focused regime transport (IFR) to guide the beam. In a racetrack configuration, the ion channel must survive for as long as 400 nsec, a time long compared with the characteristic time for a bare ion channel to expand due to its own space charge. The FRIEZR code has been modified to treat long-time-scale ion motion. Plasma electron and ion dynamics are included, and an artificially low ion mass (hydrogen instead of xenon) is used with an appropriately rescaled pulse length. We first investigated whether plasma electrons from the wall could neutralize the ion space charge and slow the expansion of the channel after the beam pulse has ended; however, the inclusion of these electrons was not very effective. Somewhat more promising results were obtained when the beam created part of the channel itself, thus replenishing part of the channel after each recirculation. This strategy could be employed by raising the background gas pressure to a few mtorr. We also made analytical estimates of the characteristic time for a bare channel to drift off-axis due to electrostatic image charges in the wall. Although this effect is small, it cannot be readily corrected for since the electrostatic equilibrium is inherently unstable. (Joyce, Hubbard, Fernsler)

**F. Erosion of Electron Beams in the RLA Accelerator:** The ELBA simulation code has been used to study inductive erosion, beam drift and current loss in both straight and curved sections of the RLA. The observed erosion rate in straight sections agrees well with analytical estimates and 2-D FRIEZR simulations. In curved sections, the erosion rate is typically 30-50% higher. If the vertical field  $B_y$  is well-matched to the nominal beam energy and bend radius of curvature, inductive energy loss at the beam head may cause the beam centroid in that region to drift to the inside. Plasma electrons are ejected along the vertical field lines, but this complicated

process does not appear to degrade the beam significantly. A 10% mismatch in the vertical field  $B_y$  causes modest drifts in the beam centroid and has a small effect on the erosion rate.

Beam transport simulations of a "recirculated" RLA beam have been carried out by using an expanded and weaker channel and a higher beam energy. As expected, the inductive erosion rates are small, but significant drifting in the beam centroid is often observed because the channel does not provide a strong centering force. (Hubbard, Joyce, Slinker)

#### G. Atomic and Plasma Surface Interactions in Accelerators and IFR

**Cells:** This paper summarizes the various atomic physics processes which may occur in accelerators and IFR cells. Beam impact ionization of the ambient or outgassed species is negligible for the SLIA but may be important for the betatron and RLA. Accelerated plasma electrons and ions may impact the wall, creating a substantial surface plasma. In addition, fast neutral particles, creating by charge exchange with plasma ions, may also impact the wall surface. In induction accelerators, these plasmas can lead to undesirable electrical breakdown in the accelerating gaps, a process which has been observed experimental in the laser-guided ATA accelerator. Both analytical and ab-initio computer models are currently being explored to treat these processes. (Ali)

## ELBA - A Three-Dimensional Particle Simulation Code\*

Glenn Joyce, Jonathan Krall, Steve Slinker

Beam Physics Branch, Plasma Physics Division  
Naval Research Laboratory

### INTRODUCTION:

The study of the interaction of relativistic electron beams with plasmas and with external magnetic field configurations has required the development of sophisticated particle simulation codes. We developed the FRIEZER code to look at axisymmetric problems of beam propagation in the Ion Focus Regime (IFR). A number of investigations were made using the models integrated into that code. We are now progressing to the study of three-dimensional phenomena associated with beam propagation through diffuse plasmas and with beam transport in compact accelerators. We have developed a three-dimensional code, ELBA, to investigate the physics of some of these phenomena. The ELBA code is based largely on FRIEZER with the addition of three-dimensional electromagnetic fields. It is formulated in the  $(r, \theta, \zeta = ct - z)$  coordinate system, has fully relativistic beam and plasma particles, and is fully electromagnetic. In addition, we have included the capability of simulating the transport of particle beams around bends in the limit of a large radius of curvature. The latter formulation is based on a mapping scheme developed by Alex Friedman. The mapping algorithm does not depend on the radius of curvature, but the electromagnetic fields include an expansion to first order in the inverse aspect ratio of the the simulation waveguide radius to the radius of curvature.

### GENERAL ISSUES:

Because of the nature of high energy electrons, a number of conventions have been adopted for their study which are not usually found in particle simulation codes. It is convenient to replace the space and time variables  $z$  and  $t$  by  $\zeta = ct - z$  and  $t$ . Relativistic beam particles, in terms of these variables, exhibit very slow motion in the axial,  $\zeta$ , direction. A beam particle moving exactly at the speed of light would have a constant value of  $\zeta$ . The actual motion will result in a slow increase in  $\zeta$  position of

the particle depending on its energy and perpendicular velocity. The plasma particles on the other hand appear to be streaming by the beam at roughly the speed of light. We are usually interested primarily in the beam dynamics so the  $\zeta, t$  coordinates are generally well-suited for our use. A second consequence of the  $\zeta, t$  coordinates concerns the boundary conditions for the electromagnetic fields. No information can flow forward in these variables so the propagation of all electromagnetic waves is toward larger  $\zeta$ . As a result, we can predetermine the values of the electromagnetic fields at the front end of the simulation system and they will remain unchanged by the beam.

The fact that we do not have to treat information moving in the forward direction allows us to handle particle data in a particularly simple way. The simulation region is divided axially into a number of "slices" with the slice length corresponding to the grid size along the  $\zeta$  axis. The point  $\zeta=0$  is generally associated with initial position of the beam head and  $\zeta=\zeta_{\max}$  is associated with the beam tail. At any given time each particle, whether it is a beam or plasma particle, is associated with a particular slice. As time progresses, the particle either stays in that slice or moves to the next slice at larger  $\zeta$ . A particle at any given slice cannot be influenced by a particle in another slice which is nearer the tail beam. As a result, not all particles need to be in the computer simultaneously. At each time step we can begin with the first slice, read the particle variables for this slice (with some associated field, charge, and current density quantities), calculate the electromagnetic fields for the slice, push the particles, calculate the charge and current densities, store the particle, density, and field information on disk and begin with the next slice working our way from the front to the back of the beam. As particles move from slice to slice, they are marked as having moved to next slice and stored appropriately. The marking process requires that we must do a particle sort at each time step and at each slice. The sort is into two regions; the particles which remain in the slice, and those which move to the next slice. At the time that we do the sort, we also handle particles which have crossed the radial simulation boundary. Normally, we excise these particles from the simulation. As a result of this buffering system,

we can simulate beams with an almost unlimited number of particles although we pay a price in I/O. A single time step represents the processing of all the slices in the simulation region from the beam head to the beam tail. No particle can move to a slice nearer the beam head since the slice "velocity" is c. The beam particles slowly move from slice to slice while the plasma particles change slices frequently. In order to make the bookkeeping simple, we choose the time step to be smaller than  $\Delta\zeta/2c$ . This constraint is also imposed on us by the field solver.

#### ELECTROMAGNETIC FIELDS:

We solve the electromagnetic fields from a representation of the scalar and vector potentials. The equations are solved in much the same manner as FRIEZR using the gauge  $\nabla_{\perp} \cdot A_{\perp} = 0$ . Here,  $A_{\perp}$  is the component of the vector potential perpendicular to the  $\zeta$  axis. The fields are solved in much the same way as in FRIEZR. We solve mode by mode in a Fourier transformed space where the Fourier transform is taken in the azimuthal direction. We will discuss the electromagnetic field solution in more detail in a more complete paper on the code.

We have chosen a radial grid which is nonlinear in the  $r$  coordinate. Since the beam particles normally lie near the axis of the system, it is convenient to have the grids more closely spaced here than near the walls. An evenly spaced grid in the coordinate  $u = \ln(1 + r^2)$  has that property. Near the axis  $u \sim r^2$ , which approximates a constant current density grid, while for large  $r$  the grid spacing increases exponentially. Our experience is that this grid works quite well, although we must be careful in its implementation.

#### INITIAL CONDITIONS:

Although the choice of the  $(\zeta, t)$  coordinate system simplifies the boundary conditions at  $\zeta=0$ , some decisions must be made about the laboratory  $z=0$  and the initial conditions. The simplest assumption is that it is not important where the beam is initially. In this case, the beam charge can be turned on adiabatically, and the long term behavior of the system can be studied. Usually, however, we want to simulate the beam

entering a region of interest from some other region and we must decide how to treat ( $z=0, t=0$ ). After a number of trials, we have implemented the following initialization steps. At  $t=0$ , we assume that the head of the beam is at  $z=0$  and that the rest of the beam is out of the region of interest. For initial conditions, we choose a time independent solution for the electromagnetic fields appropriate to a beam in a vacuum. The plasma is chosen to be charge neutral and cold. As the beam enters the simulation region ( $z>0$ ), we push the beam particles, but for the portion of the beam remaining outside the simulation region, we freeze motion in the radial direction and allow the beam to free stream in the  $\zeta$  direction. In order to avoid discontinuities at the  $z=0$  boundary, we allow the plasma to react to the fields in both regions of the simulation. This scenario provides a reasonable model for the entrance of the beam into a transport system.

#### CONCLUSIONS:

The ELBA code has proved to be a useful tool in a number of studies of relativistic beam transport and propagation. The coordinate system limits its applicability to beams which are moving at roughly the speed of light. We have restricted the boundary conditions to be those of a perfectly conducting cylinder so that the electromagnetic fields can be solved quickly. We have usually opted for speed and simplicity over generality. The inclusion of bends is still in an experimental stage in that we are continuing to study and make improvements in the algorithm.

\*Work supported by the Defense Advanced Research Projects Agency, ARPA Order No. 4395, Amendment 80, monitored by Naval Surface Warfare Center.

# Stability Regimes in a Rotating Quadrupole Focusing Accelerator\*

C. M. Tang, P. Sprangle, J. Krall, P. Serafini<sup>†</sup> and F. Mako<sup>‡</sup>

Beam Physics Branch, Plasma Physics Division  
Naval Research Laboratory, Washington, DC 20375-5000

A number of recent high current accelerator configurations utilize strong focusing fields. These fields, consisting of a rotating quadrupole field (or stellarator field) and an axial guide field, increase considerably the energy mismatch tolerance of the device and provide confining forces against the beam space charge forces.<sup>1,2</sup> Two such devices are the modified betatron accelerator<sup>3</sup> and the spiral line induction accelerator (SLIA).<sup>4</sup> The SLIA, to be constructed by Pulse Sciences, Inc., will utilize the strong focusing for transport along the curved sections of the beam line between the accelerating cavities.

The use of strong focusing fields has a potential difficulty in that they can lead to various types of beam instabilities.<sup>5-7</sup> We find that the electron beam centroid can be i) orbit unstable independent of the waveguide modes, ii) three-wave unstable or iii) fully stable. The conditions for each regime are presented in the limit of zero beam current. Algebraic expressions for the growth rate in each of the three-wave unstable regimes are obtained, and they are in general agreement with the expressions given in Ref. 8.

**DISPERSION RELATION.** The external magnetic field consists of an axial guide field  $B_o$ , and a rotating quadrupole field ( $B_{qx}$ ,  $B_{qy}$ ), where

$$B_{qx} = -B_q k_q (x \sin k_q z - y \cos k_q z), \quad B_{qy} = B_q k_q (x \cos k_q z + y \sin k_q z), \quad (1a-b)$$

$B_q k_q$  is the quadrupole gradient, and  $k_q$  is the wave number of the quadrupole field. The representation for the quadrupole field in Eqs. (1a-b) is valid near the z-axis, i.e.,  $(x^2 + y^2)^{1/2} \ll \lambda_q/2\pi$ . In equilibrium, the electron beam travels along the axis of a circular waveguide at velocity  $v_o$  and is monoenergetic with  $\gamma_o = (1 - \beta_o^2)^{-1/2}$ , where  $\beta_o = v_o/c$ .

We assume the electron beam propagates within a perfectly conducting cylindrical waveguide of radius  $r_g$ . We include induced image charges and currents due to the displaced beam. Both the beam radius and beam centroid displacement are assumed to be small in comparison to the waveguide radius.

We expect  $TE_{11}$  mode to have the largest growth rate, because its electric field peaks on axis. Its vector potential can be written as  $\mathbf{A} = \mathbf{A}_{11}(r, \theta) \exp\{i(kz - \omega t)\} + c.c.$ , where  $\omega$  is the radian frequency,  $k$  is the wave number and c.c. denotes the complex conjugate. The boundary condition, requiring the tangential component of the electric field to vanish on the perfectly conducting waveguide surface, gives the condition  $J'_1(\mu_{11} r_g) = 0$ , where  $\mu_{11} r_g$  is the smallest positive zero of Bessel function  $J'_1$ .

\* Work supported by Defense Advanced Research Projects Agency, ARPA Order No. 4395, Amendment 80, monitored by Naval Surface Warfare Center.

† Northeastern University, Boston, MA 02115

‡ FM Technologies, Inc., Alexandria, VA 22304

When the wave equation is solved simultaneously with the particle dynamics equation, we obtain the following dispersion relation

$$W_r W_l W_u W_s = k_b^2 \left[ (k + k_q - \omega/v_o)^2 D_- W_r + (k - \omega/v_o)^2 D_+ W_l \right], \quad (2)$$

where  $k_b^2 = 2(I_b/17)\mu_{11}^2/(\gamma_o(\mu_{11}^2 r_g^2 - 1)J_1^2(\mu_{11} r_g))$ ,  $I_b$  is the beam current in kA,  $W_r = \omega^2/c^2 - k^2 - \mu_{11}^2$  and  $W_l = \omega^2/c^2 - (k + k_q)^2 - \mu_{11}^2$  are contributions from the right-hand circularly polarized (RHCP) and left-hand circularly polarized (LHCP)  $TE_{11}$  waveguide modes respectively,  $W_s = K^2 - (d_1^2 + d_2^2)$  accounts for the two stable beam modes,  $W_u = K^2 - (d_1^2 - d_2^2)$  admits the two potentially unstable beam modes,  $d_1^2 = K_2^2 + K_1^2/2$ ,  $d_2^2 = ((K_2^2 + K_1^2/2)^2 - (K_2^4 - K_3^4))^{1/2}$ ,  $K = k - \omega/v_o + k_q/2$ ,  $D_{\pm} = K^2 \mp K_1 K - K_2^2$ ,  $K_1 = K_o - k_q$ ,  $K_2^2 = (K_o - k_q/2)k_q/2 - k_s^2$ ,  $K_3^2 = K_q k_q$ ,  $K_o = |\epsilon|B_o/\beta_o\gamma_o m_o c^2$  is the relativistic cyclotron wave number associated with the axial field,  $K_q = |\epsilon|B_q/\beta_o\gamma_o m_o c^2$  is the relativistic cyclotron wave number associated with the rotating quadrupole field and  $k_s = (2(I_b/17)/(\beta_o^2\gamma_o^3 r_g^2))^{1/2}$ . Equation (2) agrees with the dispersion relation in Ref. (6) with the vertical field set to zero.

**STABILITY REGIMES AND ANALYTICAL GROWTH RATE EXPRESSIONS.** The dispersion relation, Eq. (2), contains i) a region of orbital instability, ii) two regions of three-wave instability and iii) two regions of stability. The stability diagrams are obtained in  $(k_q, K_o)$  space for given values of  $\gamma$ ,  $r_g$  and  $B_q k_q$ .

- i) **Orbit Unstable Regime.** The electron beam in this configuration can be orbit and three-wave unstable when  $(d_1^2 - d_2^2) \leq 0$ . The unstable values of  $K_o$  are

$$K_{crit,2} \equiv k_q/2 - 2K_q \leq K_o \leq K_{crit,3} \equiv k_q/2 + 2K_q, \quad (3)$$

where  $K_q = |\epsilon|B_q/\beta_o\gamma_o m_o c^2$  and  $K_o = |\epsilon|B_o/\beta_o\gamma_o m_o c^2$ . Equation (3) is in agreement with the stability condition of Ref. 1 in the limit of straight cylindrical geometry and zero beam current, the stability condition of Ref. 2 in the limit of perfectly conducting walls, and the condition for beam envelope stability of Ref. 9 in the limit of zero space charge.

- ii) **Three-Wave Unstable Regimes.** Numerical solutions of the dispersion relation (2) indicate that the three-wave instability occurs when the RHCP waveguide mode [or the LHCP waveguide mode] intersects, in the  $(\omega, k)$  plane, the appropriate beam mode given by  $W_u = 0$  and  $(d_1^2 - d_2^2) < 0$ . For  $K_o > K_{crit,2}$ , the three-wave is unstable (Region I) when the RHCP waveguide mode intersects the beam line  $\omega/v_o = (k + k_q/2) + \sqrt{d_1^2 - d_2^2}$ . For  $K_o < K_{crit,3}$ , the three-wave is unstable (Region II) when the RHCP waveguide mode intersects the beam line  $\omega/v_o = (k + k_q/2) - \sqrt{d_1^2 - d_2^2}$ .

We obtain algebraic expressions for the peak growth rates  $Im(\delta\omega/c)$ , where

$$(\delta\omega/c)^2 \simeq \mp k_b^2 (k - \omega_1/v_o)^2 D_{\pm} \Big|_{\omega = \omega_1 \pm \Delta\omega_2} [8\beta_o^2 c^4 \omega_1 d_2^2 (d_1^2 - d_2^2)]^{-1}, \quad (4)$$

where  $\omega_1 = \sqrt{k^2 + \mu_{11}^2}c$ ,  $\omega_2 = v_o(k + k_q/2)$ ,  $\Delta\omega_2 = v_o\sqrt{d_1^2 - d_2^2}$ ,  $D_{+}|_{\omega=\omega_2 \pm \Delta\omega_2} = (\Delta\omega_2/v_o)^2 \pm K_1(\Delta\omega_2/v_o) - K_2^2$  and the top and bottom signs in (4) refer to the three-wave unstable regions I and II respectively.

- iii) Three-Wave Stable Regime for  $K_o < K_{crit,2}$ . Stability is achieved when the waveguide cut off frequency  $\mu_{11}c$  is sufficiently large so that intersection with either of the beam lines, defined by  $W_u = 0$  cannot be achieved. The three-wave is stable if  $q\mu_{11} \geq k_q + 2(d_1^2 - d_2^2)^{1/2}$ , where  $q = (4/(\gamma_o^2 - 2))^{1/2}$ . For  $k_q < q\mu_{11}$ , and defining  $\zeta = k_q^2(1 + 8K_3^4/k_q^2f) - 2f$  and  $f = q\mu_{11}(k_q - q\mu_{11}/2)$ , the electron beam is stable for the following situations:

- a) for  $f > 0$  and  $\zeta > 0$ , the stable range of  $K_o$  is given by

$$K_{crit,1} \equiv k_q/2 - \zeta^{1/2}/2 < K_o < K_{crit,2}, \quad (5a)$$

- b) for  $f < 0$  and  $\zeta > 0$ , the stable values of  $K_o$  are

$$K_o < K_{crit,1} \equiv \text{smaller of } (k_q/2 - \zeta^{1/2}/2, K_{crit,2}), \quad (5b)$$

- c) for  $f < 0$  and  $\zeta < 0$ , all values of  $K_o > K_{crit,2}$  are stable.

- iv) Three-Wave Stable Regime for  $K_o > K_{crit,3}$ . The three-wave interaction is also stable when the RHCP waveguide mode does not intersect  $\omega/v_o = (k + k_q/2) - \sqrt{d_1^2 - d_2^2}$  for  $K_o > K_{crit,3}$ . This occurs when  $q\mu_{11} \geq k_q + 2(d_1^2 - d_2^2)^{1/2}$ , for which there are two stable cases:

- a) for  $k_q < q\mu_{11}$ , the stable range of  $K_o$  is  $K_o > K_{crit,3}$ ,  
 b) for  $k_q > q\mu_{11}$ , the stable range of  $K_o$  is

$$K_o > K_{crit,4} \equiv k_q/2 + \zeta^{1/2}/2. \quad (6)$$

In the limit of small quadrupole gradients, large  $\gamma_o$  and  $K_o \gg K_{crit,3}$ , the stability condition<sup>10</sup> is approximately  $K_o \geq k_q - \mu_{11}/\gamma_o$ .

The various operating regimes are illustrated as functions of  $k_q$  and  $K_o$  in Fig. 1, for  $\gamma_o = 5$ ,  $r_g = 3$  cm and quadrupole gradient  $B_q k_q = 200$  G/cm. Since the stability boundaries are obtained in the limit of zero beam current, the area of the two stable regions will shrink slightly as the current is increased.

To operate in the stable regime with  $B_o = 0$ , both the maximum allowable quadrupole gradient and the quadrupole wave number must decrease for increasing beam energy. Figure 2 is a plot of maximum quadrupole gradient versus  $\gamma_o$  for a fixed guide field  $B_o = 5$  kG,  $r_g = 3$  cm and two different values of quadrupole wave number:  $k_q = 0.1$  cm<sup>-1</sup> (—) and  $k_q = 0.05$  cm<sup>-1</sup> (---).

**CONCLUSIONS.** Analytic stability boundaries and algebraic expressions of the growth rate are in agreement with numerical solutions of the dispersion relation. These results

suggest that the SLIA proof of concept experiment can operate entirely in the stable regime.

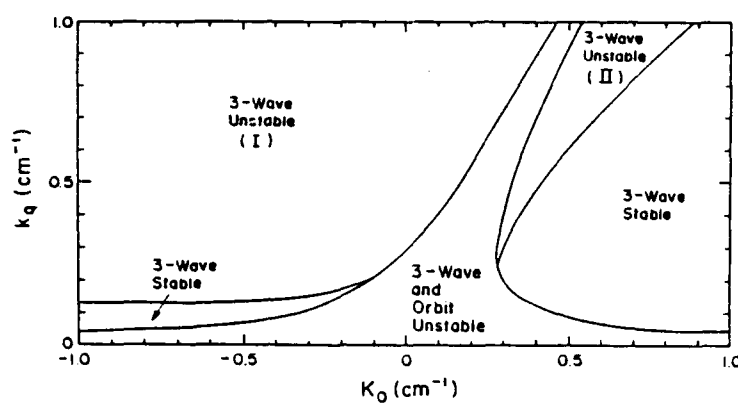


Fig. 1. Plot of the various operating regimes for  $\gamma_0 = 5$ ,  $r_g = 3 \text{ cm}$  and quadrupole gradient  $B_q k_q = 200 \text{ G/cm}$ .

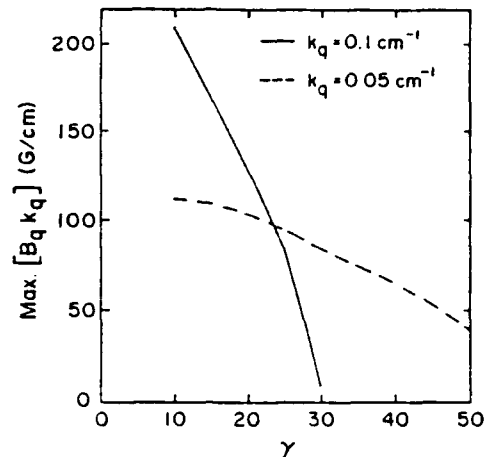


Fig. 2. Plot of maximum quadrupole gradient versus  $\gamma_0$  for guide field  $B_0 = 5 \text{ kG}$  and  $r_g = 3 \text{ cm}$ .

#### REFERENCES.

1. C. W. Roberson, A. Mondelli and D. Chernin, Phys. Rev. Lett. 50, 507 (1983).
2. P. Sprangle and C. A. Kapetanakos, Part. Accel. 18, 203 (1986).
3. J. Golden, J. Pasour, D. E. Pershing, T. Smith, F. Mako, S. Slinker, F. Moro, N. Orrick, R. Altes, A. Fliflet, P. Champney and C. A. Kapetanakos, IEEE Trans. on Nucl. Sci. NS-30, 2114 (1983).
4. A. Mondelli, D. Chernin, S. D. Putnam, L. Schlitt and V. Bailey, Proc. Sixth Intl. Conf. on High Power Part. Beams (Osaka, Japan), (1986); V. Bailey, L. Schlitt, M. Tiefenback, S. Putnam, A. Mondelli, D. Chernin and J. Petillo, Proc. of the 1987 IEEE Particle Accel. Conf., 920 (1987).
5. B. Levush, T. M. Antonsen, W. M. Manheimer and P. Sprangle, Phys. Fluids 28, 7 (1985).
6. T. P. Hughes and B. B. Godfrey, Phys. Fluids 29, 1698 (1986).
7. C. M. Tang, P. Sprangle, J. Krall, P. Serafim and F. Mako, submitted to Part. Accel.
8. B. B. Godfrey and T. P. Hughes, MRC/ABQ-R-1011 (Mission Research Corp., Albuquerque, NM, 1988).
9. D. Chernin, Part. Accel. 24, 29 (1988).
10. Private communications with D. Chernin and T. Hughes.

THREE-DIMENSIONAL SIMULATIONS OF ELECTROMAGNETICALLY STABLE AND  
UNSTABLE REGIMES IN THE SPIRAL LINE INDUCTION ACCELERATOR\*

J. KRALL, C. M. TANG and G. JOYCE

Naval Research Laboratory  
Beam Physics Branch  
Plasma Physics Division  
Washington, DC 20375-5000

Magnetic transport of high-current electron beams is an important problem in induction accelerator physics. One such accelerator is the spiral line induction accelerator (SLIA)<sup>1</sup>, which uses solenoidal focusing in the straight sections and both solenoidal and stellarator (helical quadrupole) focusing in the curved sections. The stellarator fields, which focus the space charge of the beam over a large energy bandwidth, make the high-current beam subject to electromagnetic instabilities, such as the three-wave instability.<sup>2-4</sup>

For the present numerical study we use the ELBA code, a three-dimensional particle code which simulates a beam propagating within a cylindrical metallic pipe. The full set of Maxwell's equations along with the full relativistic motion of the beam particles are included. The beam is initially matched to the field configuration to minimize initial oscillations. This matched configuration is calculated by STELMAT<sup>5</sup>, which was adapted for use in ELBA.

ELECTROMAGNETIC THREE-WAVE INSTABILITY

The electromagnetic three-wave instability has been studied by various authors.<sup>2-4</sup> Of interest here are theoretical predictions of three-wave stable field configurations.<sup>3,4</sup> In the limit of low current ( $I_b \rightarrow 0$ ), analytic expressions for stability boundaries in  $(k_q, B_z)$  space have been obtained<sup>4</sup>, where  $k_q = 4\pi/\lambda_p$  is the wavenumber of the helical quadrupole fields,  $\lambda_p$  is the quadrupole pitch length, and  $B_z$  is the axial magnetic field. These boundaries are functions only of the amplitude of the quadrupole gradient,  $B_q k_q$ , the relativistic factor for the beam,  $\gamma$ , and the waveguide (pipe) radius,  $r_g$ . Stability boundaries are plotted in Fig. 1 for parameters of interest for the proposed SLIA proof-of-concept experiment (PoCE):  $B_q k_q = 200$  g/cm,  $\gamma = 7$ , and  $r_g = 3$  cm. The operating point for the PoCE is indicated by an "x" in the figure. Note that the diagram encompasses two three-wave unstable regimes, which are physically distinct, an orbit unstable regime and two stable regimes. Note that the condition for orbit instability in this limit, which recovers an earlier result<sup>6</sup>, is identical to the condition for unstable beam envelope oscillations, derived for such beams in reference 7. Note that we consider only  $k_q > 0$ , which indicates right-handed helicity in the quadrupole windings. By symmetry,  $(k_q, B_z)$  is equivalent to  $(-k_q, -B_z)$ .

\*Work supported by the Defense Advanced Research Projects Agency.

Theoretical results suggest that the PoCE can operate entirely in the stable regime. They also suggest that as  $\gamma$  is increased, the conditions for stability become more restrictive, forcing operation at longer pitch lengths and lower quadrupole gradients.<sup>4</sup> This may not present a problem as beam focusing requirements are generally less stringent as  $\gamma$  is increased.

## NUMERICAL RESULTS

Simulations have been performed for parameters typical of the SLIA PoCE:  $I_b = 10$  kA, normalized RMS emittance,  $\epsilon_{N,RMS} = .158$  cm-rad,  $r_g = 3$  cm,  $B_q k_q = 200$  G/cm,  $k_q = 0.1$  and  $B_z = 5$  kG. We simulated both  $\gamma = 7$  and  $\gamma = 13$ , corresponding to the beam energies for the initial and final stellarator sections of the PoCE. The case of  $B_z = -5$  kG at  $\gamma = 7$ , corresponding to the smaller (and less useful) stable regime in Fig. 1, was also simulated. Stable behavior was observed in all three cases. In order to observe transitions between the various stability regimes, we set  $k_q = 0.5$  cm<sup>-1</sup> and  $\gamma = 7$  and considered  $B_z = 1, 2, 4, 4.5$  and  $6$  kG. The ( $k_q, B_z$ ) parameter space locations for these runs are noted in Fig. 1. The results are listed in Table 1. Shown are theoretical and numerical values for the growth rate and peak frequency for the electromagnetic TE<sub>11</sub> mode.

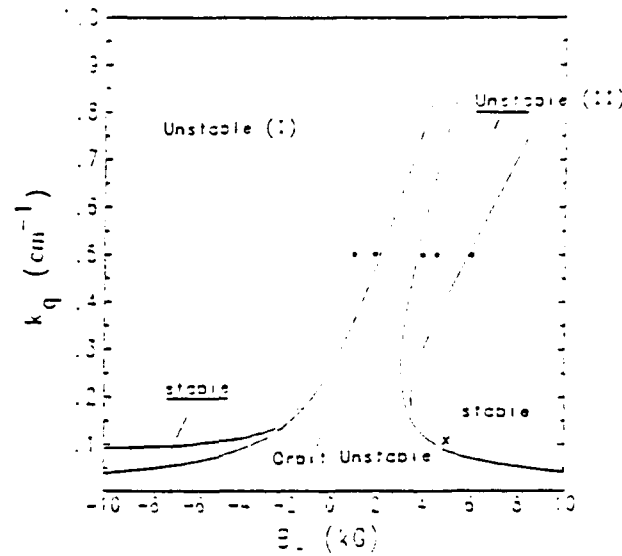


Fig. 1 Stability diagram for beam energy  $\gamma = 7$ , quadrupole gradient  $B_q k_q = 200$  G/cm and waveguide radius  $r_g = 3$  cm.

<u><math>B_z</math> (kG)</u>	<u>Linear Theory</u>		<u>Simulation</u>	
	<u><math>\Gamma</math> (cm<sup>-1</sup>)</u>	<u><math>\omega_{peak}/c</math> (cm<sup>-1</sup>)</u>	<u><math>\Gamma</math> (cm<sup>-1</sup>)</u>	<u><math>\omega_{peak}/c</math> (cm<sup>-1</sup>)</u>
1.0	.0334	0.71	0.009	0.75
2.0	.0438	1.03	0.019	0.94
4.0	orbit-unstable	-	orbit-unstable	-
4.5	.0266	0.84	0.020	0.83
6.0	stable	-	stable	-

Table 1. Theoretical and numerical values of peak growth rates and peak frequencies for varying  $B_z$ .

Growth rates were measured by analyzing the TE<sub>11</sub> mode, for which the  $B_z$  and  $E_r$  components may be "projected out" from the electromagnetic spectrum in a straightforward manner. The  $B_z$  component of the TE<sub>11</sub> mode is then decomposed via FFT into discrete wavenumbers,  $k$ . The growth rate is then obtained as a function of  $k$  for those cases where an unstable mode grew above the background "noise". Similarly, growth rates may be obtained as a function of frequency,  $\omega$ . Because our simulation takes place in a coordinate system,  $(r, \theta, \zeta = ct - z)$ , that moves with the beam, the growth rates that result from this analysis of the data are  $\Gamma = \text{Im}(\omega/c - k)$ . This corresponds to the theoretical result only in the case that  $\text{Im}(k) = 0$  as was assumed in obtaining the theoretical growth rates given in Table 1.

As an example, the numerically measured TE<sub>11</sub> mode at  $\omega/c = 0.83 \text{ cm}^{-1}$  is plotted on a logarithmic scale versus position,  $z$ , in Fig. 2 for the  $B_z = 4.5 \text{ kG}$  case. From this plot, the mode appears to saturate at  $z = 350 \text{ cm}$ . This saturation may be a numerical effect due to the fact that the particle simulation is inherently noisy. A carefully scaled parameter study would be required to determine actual saturation levels for the instability.

Several aspects of the simulation results deserve comment:

1) To minimize computational expense, the typical simulation, which takes place in the "beam frame", was of a short ( $< 1 \text{ m}$ ) beam propagating over a distance of 2-10 meters. In the PoCE, the pulse length is  $\approx 25 \text{ m}$  and the interaction length (curved section) is  $\approx 2.5 \text{ m}$ .

2) Apparent saturation of the instability was observed in each of the three-wave unstable cases. This was associated with a beam centroid displacement in the 1-2 mm range, an emittance increase of 20-100% and, in most cases, the onset of current loss. The exact saturation mechanism, which may be due to numerical effects or to selective loss of beam particles, was not determined.

3) The spectrum of unstable modes was typically much broader than predicted by the linear theory. This was especially pronounced in the  $B_z = 1 \text{ kG}$  and  $B_z = 2 \text{ kG}$  cases, where the growth rates were significantly lower than predicted. The broad spectra are not surprising in that the beam radius,  $r_b = 1-2 \text{ cm}$ , is much larger than is assumed in the theory.

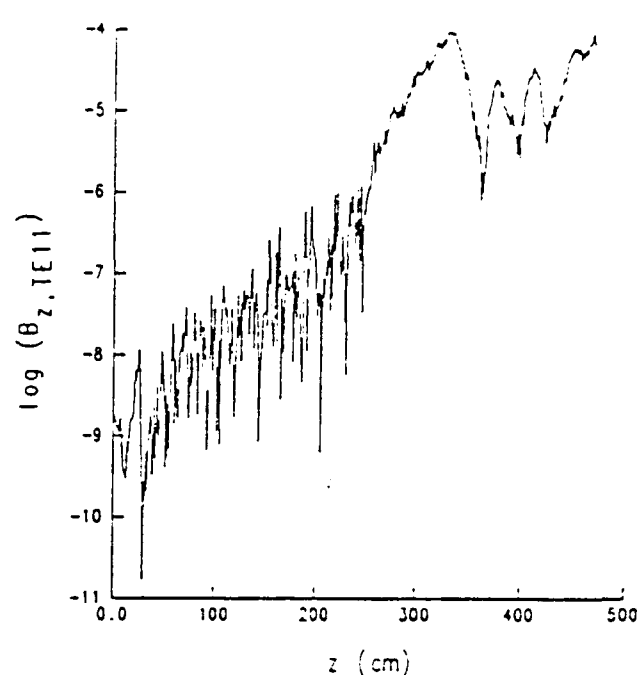


Fig. 2 The Fourier component of  $B_z, \text{TE11}$  at  $\omega/c = 0.83 \text{ cm}^{-1}$  plotted versus  $z$  for the  $B_z = 4.5 \text{ kG}$  case.

4) For the run at  $B_z = 4$  kG, orbit instability was observed as predicted by a numerical solution of the dispersion relation. This result disagrees with Fig. 1, which is derived in the zero current limit. As beam current is increased, the stability boundaries shift in such a way that the unstable regions become larger. At  $I_b = 10$  kA, the orbit unstable regime encompasses the  $B_z = 4$  kG point, which is close to the orbit unstable boundary at zero current. In this case, the orbit instability caused severe disruption of the beam envelope, with the major radius of the beam ellipse expanding to make contact with the wall within the first meter of propagation.

5) Further runs at PoCE parameters,  $\gamma \leq 13$ ,  $k_q = 0.1$ ,  $B_z = 5$  kG and  $100$  G/cm  $\leq B_q k_q \leq 200$  G/cm, were stable in all cases.

## CONCLUSIONS

In this study, we have used electromagnetic particle simulation to confirm and clarify the theoretical results of references 2-4. We have seen that the stability boundaries outlined in reference 4 are good predictors of behavior in the simulations. More importantly, we have verified that the three-wave stable regime, initially discussed in reference 3, lies in a region of parameter space suitable for the PoCE. This regime appears at  $B_z > 0$  in Fig. 1. Note that with our sign convention,  $B_z > 0$  corresponds to what is called the "reversed field" case in reference 3. Two minor departures from the linear theory were found. Firstly, unstable cases generally showed lower growth rates and broader spectra than expected. Secondly, apparent saturation, associated with emittance growth and the onset of beam loss, was observed in each three-wave unstable case. Stable behavior was observed in both stable regimes. Finally, these simulations confirm theoretical predictions<sup>3,4</sup> that the SLIA proof of concept experiment can operate entirely in the stable regime.

## REFERENCES

1. A. Mondelli, D. Chernin, S. D. Putnam, L. Schlitt and V. Bailey, Proc. Sixth Intl. Conf. on High Power Particle Beams (Osaka, Japan), (1986); also V. Bailey, L. Schlitt, M. Tiefenback, S. Putnam, A. Mondelli, D. Chernin and J. Petillo, Proc. 1987 IEEE Part. Accel. Conf., 920 (1987).
2. T. P. Hughes and B. B. Godfrey, Phys. Fluids 29, 5 (1986).
3. D. Chernin and T. P. Hughes (private communication).
4. C. M. Tang, P. Sprangle, J. Krall, P. Serafim and F. Mako, to be published; also these proceedings.
5. D. Chernin (private communication).
6. C.W. Roberson, A. Mondelli and D. Chernin, Phys. Rev. Lett. 50, 507 (1983).
7. D. Chernin, Part. Accel. 24, 29 (1988).

THREE-DIMENSIONAL SIMULATIONS OF BEAM TRANSPORT AND EMITTANCE  
GROWTH IN THE SPIRAL LINE INDUCTION ACCELERATOR\*

J. KRALL and G. JOYCE

Naval Research Laboratory  
Beam Physics Branch  
Plasma Physics Division  
Washington, DC 20375-5000

Magnetic transport of high-current electron beams is a problem of increasing importance for induction accelerator physics. An example is the spiral line induction accelerator (SLIA)<sup>1</sup>, which uses solenoidal focusing in the straight sections and both solenoidal and stellarator (helical quadrupole) focusing in the curved sections. Potential difficulties with this scheme arise from the need to transport the beam through transitions from solenoidal to stellarator focusing on each turn. The need here is to minimize or eliminate emittance growth through each transition.

The present numerical study is the product of ELBA<sup>2</sup>, a three-dimensional particle code recently developed at NRL. ELBA simulates a beam propagating within a cylindrical metallic pipe. The full set of Maxwell's equations and the full relativistic motion of the beam particles are included. The beam is matched to the field configuration to minimize initial oscillations. This matched configuration is calculated by STELMAT<sup>3</sup>, which was adapted for use in ELBA.

BEAM TRANSPORT IN STELLARATOR FIELDS

Previous studies of beam transport in stellarator-focused accelerators have been primarily concerned with stellarator-betatron configurations, where transitions from stellarator to solenoidal focusing are not required as in the SLIA. This matching problem is ideally solved through the use of focusing elements which somehow convert a matched beam in solenoidal fields (circular cross section) into a matched beam in the stellarator fields (elliptical cross section). Recent studies<sup>4</sup> have suggested strategies through which this may be accomplished, but without directly addressing the issue of emittance growth through these transitions. Intuitively, we expect configurations for which the matched beam ellipse has a high eccentricity to cause the greatest emittance growth.

In this preliminary study, we use the ELBA simulation code to transport a short slice of beam through stellarator fields typical of those discussed for the SLIA proof of concept experiment (PoCE).<sup>1,4</sup> Two significant approximations are used. Firstly we ignore curvature effects by performing the simulations in straight cylindrical geometry. Secondly we idealize the external fields, ignoring fringing fields and other realistic corrections. In each case quadrupole fields are ramped smoothly with an envelope given by

---

\*Work supported by the Defense Advanced Research Projects Agency.

$$F(z) = \frac{1}{2} \left( 1 + \tanh \left[ \frac{2(z - z_1)}{z_{\text{ramp}}} \right] \right) \quad (1)$$

where the entrance to the stellarator section is located at  $z = z_1$  and  $z_{\text{ramp}}$  is a scale length over which this function increases from 0.12 to 0.88. The quadrupole fields are "ramped down" in a similar fashion at the exit. In all cases we chose  $z_{\text{ramp}} = 6$  cm, and fixed the length of the stellarator section at  $\pi R = 751.33$  cm, where  $R = 80$  cm is the radius of curvature of the PoCE bends.

In this study, we will use an emittance definition for beams with coupled x-y motion<sup>5</sup>:

$$\varepsilon_{xy, \text{rms}} = |\Sigma|^{1/4} \quad (2)$$

where the matrix  $\Sigma$  is given by

$$\Sigma_{ij} = \langle u_i u_j \rangle - \langle u_i \rangle \langle u_j \rangle . \quad (3)$$

Here, " $\langle \rangle$ " signifies an average over the beam particles and  $i, j = 1, 2, 3, 4$  with  $u_1 = x$ ,  $u_2 = dx/dz$ ,  $u_3 = y$  and  $u_4 = dy/dz$ . The normalized, RMS emittance is  $\varepsilon_{n, \text{rms}} = \beta \gamma \varepsilon_{xy, \text{rms}}$ .

#### NUMERICAL RESULTS

We first consider a high eccentricity case. The parameters are beam current  $I_b = 10$  kA, relativistic factor  $\gamma = 7$ ,  $\varepsilon_{n, \text{rms}} = 0.158$  cm-rad, axial field  $B_z = 5$  kG, quadrupole gradient  $\nabla B_q = 198$  G/cm and quadrupole pitch length  $\lambda_p = 125.7$  cm. In this case the matched beam parameters in the stellarator section are  $R_{\text{major}} = 1.796$  cm and  $R_{\text{minor}} = 0.514$  cm so that the eccentricity, given by

$$\alpha = \left( 1 - \frac{R_{\text{minor}}^2}{R_{\text{major}}^2} \right)^{1/2}, \quad (4)$$

is  $\alpha = 0.958$ . The major and minor radii for this case are plotted versus  $z$  (propagation distance) in Fig. 1. The normalized emittance, plotted versus  $z$  in Fig. 2, shows a 47% increase.

The equilibrium beam eccentricity for these parameters can be lowered by decreasing either the pitch length or the quadrupole gradient. The emittance increase is plotted versus pitch length in Fig. 3. The eccentricity,  $\alpha$ , is also given. Plots versus quadrupole gradient are shown in Fig. 4. In both cases, the emittance variation falls below measurable levels (<3%) at  $\alpha \approx 0.65$ .

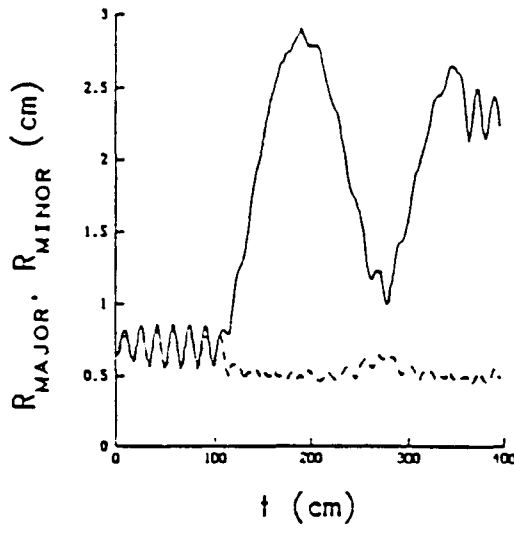


Fig. 1 Major and minor radii of the beam cross section are plotted versus propagation distance. The stellarator section is confined to  $110 \text{ cm} < z < 361.33 \text{ cm}$ .

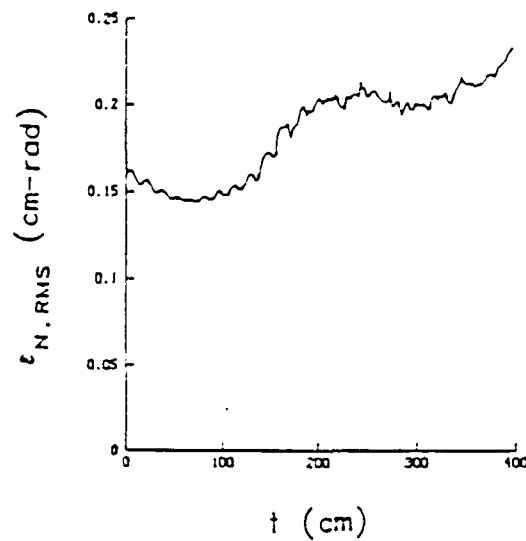


Fig. 2 Emittance versus propagation distance for the beam pictured in Fig. 1 shows emittance growth of 47%.

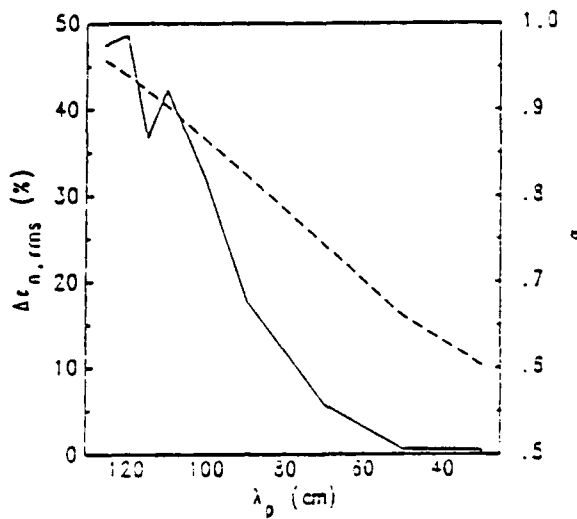


Fig. 3 Emittance growth (solid) and eccentricity (dashed) are plotted versus pitch length for the high eccentricity case.

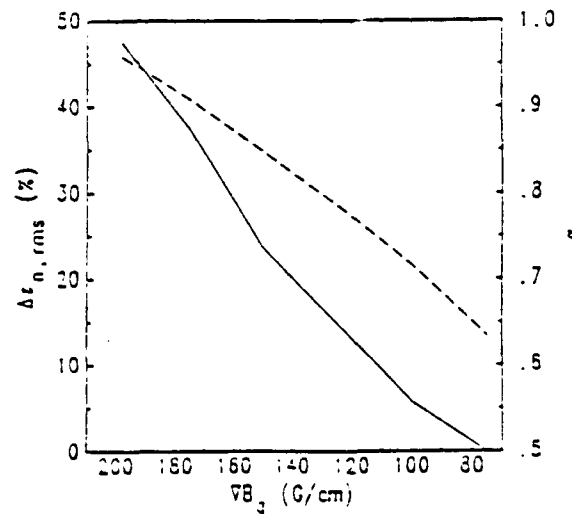


Fig. 4 Emittance growth (solid) and eccentricity (dashed) are plotted versus quadrupole gradient for the high eccentricity case.

Low eccentricity stellarator configurations have also been studied for the PoCE. A set of such parameters for each of the three PoCE bends are given in Table 1. Simulation results showed that a  $\gamma = 7$ ,  $I_b = 10$  kA,  $\epsilon_{n,rms} = 0.158$  cm-rad beam was transported through the first bend with no measurable emittance growth. In fact, as the quadrupole gradient was increased from 115.7 to 350 G/cm in this case ( $\alpha$  increasing from 0.507 to 0.835), the emittance growth remained negligible. Note that the quadrupole field period,  $\lambda_p/2 = 15$  cm, is not significantly larger than the ramp-up length for the quadrupole fields ( $z_{ramp} = 6$  cm) in this case. This suggests that higher eccentricity stellarators are tolerable when  $0(\lambda_p/2) \approx 0(z_{ramp})$ .

<u>Bend</u>	<u><math>\gamma</math></u>	<u><math>B_z</math> (kG)</u>	<u><math>\nabla B_q</math> (G/cm)</u>	<u><math>\lambda_p</math> (cm)</u>	<u><math>R_{maj}</math> (cm)</u>	<u><math>R_{min}</math> (cm)</u>	<u><math>\alpha</math></u>
1	7	4.666	115.7	31.42	.776	.669	.507
2	10	4.228	103.5	50.27	.851	.677	.606
3	13	4.446	107.6	62.83	.854	.645	.655

Table 1. Low eccentricity parameters for each of the three PoCE bends.<sup>3</sup>

Finally we performed a simulation of beam transport through three PoCE bends, using parameters given in Table 1, with  $\gamma = 7$ ,  $I_b = 10$  kA and  $\epsilon_{n,rms} = 0.158$  cm-rad. The beam, which was accelerated between each stellarator section, showed no measurable emittance growth.

## CONCLUSIONS

This preliminary study suggests that for poorly chosen parameters, transport through the stellarator focusing sections can cause emittance growth as high as 47%. Such parameters feature high eccentricity beam equilibria,  $\alpha > 0.65$ , and long pitch lengths,  $\lambda_p/2 \gg z_{ramp}$ , where  $z_{ramp}$  is the ramp-up length for the quadrupole fields. When the quadrupole field period,  $\lambda_p/2$ , is of the order of the ramp-up length for the quadrupole fields, high eccentricity ( $\alpha > 0.8$ ) stellarator sections are tolerable. Successive transitions through three low-eccentricity stellarator sections showed negligible emittance growth. It is important to keep in mind, however, that the external fields and geometry used in this study were highly idealized.

## REFERENCES

1. A. Mondelli, D. Chernin, S. D. Putnam, L. Schlitt and V. Bailey, Proc. Sixth Intl. Conf. on High Power Particle Beams (Osaka, Japan). (1986); also V. Bailey, L. Schlitt, M. Tiefenback, S. Putnam, A. Mondelli, D. Chernin and J. Petillo, Proc. 1987 IEEE Part. Accel. Conf., 920 (1987).
2. G. Joyce, J. Krall and S. Slinker, these proceedings.
3. D. Chernin (private communication).
4. A. Mondelli, D. Chernin, J. Petillo and A. Sharrits, these proceedings.
5. D. Chernin, Part. Accel. 24, 29 (1988).

NRL STUDIES OF RLA ACCELERATOR PHYSICS\*

Glenn Joyce, Richard Hubbard, and Richard Fernsler

Beam Physics Branch, Plasma Physics Division  
Naval Research Laboratory, Washington, D.C.

INTRODUCTION

One proposed design for the Recirculating Linear Accelerator is a race track configuration. An IFR channel is initially set up in the entire device using a Godfrey gun. The channel must remain intact throughout the entire experiment which lasts about 400 ns and consists of four transits of the beam around the racetrack. The behavior of the ion channel over this time period is of some concern since the channel will help guide the beam and provide space charge cancellation. A simple calculation of the time for the radius to double due to its own self forces is  $t \sim (a^2/vf m_i/m_e)^{1/2} \sim 44$  ns. This estimate is pessimistic since it assumes that the channel will maintain its shape during the acceleration time. In fact, the outer ions will travel at this rate, but the inner ions will hardly move at all so it is unlikely that the channel will maintain its shape. The behavior of the interior of the channel is probably more important than that of the channel edge.

CHANNEL NEUTRALIZATION

If the channel becomes neutralized after the passage of the beam, the time scale will become much longer, but there is a question of where the neutralizing electrons will come from. The best case scenario is that all the channel electrons will go to the chamber walls and remain there as the beam passes by. After the beam passes, the channel ions will pull the electrons back toward the channel center. However, the potential difference for a 10 ka. beam is  $\sim 230$  Kev and the kinetic energy of these electrons will be at its maximum when they are in the center of the channel so there will be little tendency for them to stop on the channel.

In order to investigate the behavior of the channel for long times, we have done a number of numerical simulations using the FRIEZR code, an axisymmetric, relativistic particle simulation code. We have performed a set of scaled "experiments" using the ion mass of Hydrogen instead of that of a heavier mass such as Xenon. Since the time scales vary as the square root of the mass ratio, we have scaled back all the times by a factor of ten. As a result, the beam length, its erosion, transport, and other properties will be incorrectly treated, but the behavior of the channel ions should give us an indication of what will happen in the actual experimental device.

We have chosen the following set of numerical parameters:

$$\begin{array}{ll} I = 8 \text{ kA} & \gamma = 10 \\ a_b = 1 \text{ m} & a_{ch} = 1 \text{ cm} \\ f = .3 & m_i/m_e = 2000 \\ l_b = 2.5 \text{ ns} & \end{array}$$

which corresponds to an "equivalent" set of experimental parameters

$$\begin{array}{ll} m_i/m_e = (100)*2000 & l_b = 25 \text{ ns} \\ \text{pulse separation} = 75 \text{ ns}. & \end{array}$$

The simulation results are summarized in Figs. 1 and 2. Over the time of two transits of the beam, the wings of the channel have spread out significantly, leaving behind a weak and narrow central core which will slowly decay away. The electrons after two transits have spread out almost uniformly across the chamber with little indication of a higher density at the channel. For our parameters, this represents about a 10% neutralization of the channel. It appears that without some strategy for replenishing the ion channel, the ion guiding effects may become too weak to be effective in providing space charge neutralization and guiding for the near term experiments.

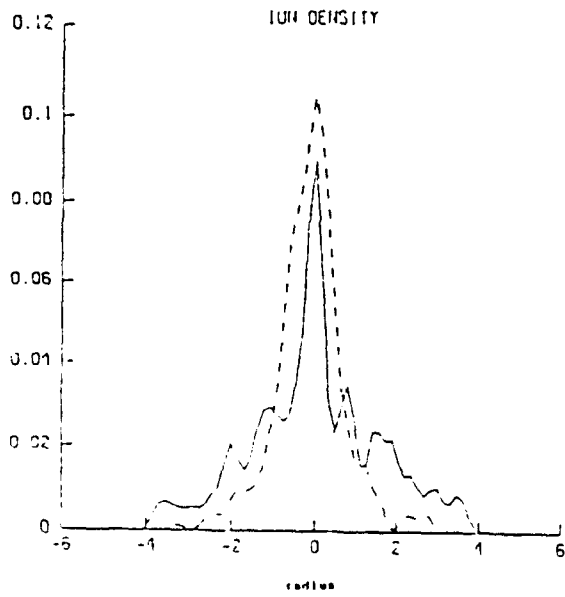


Fig. 1. Ion density vs. radius

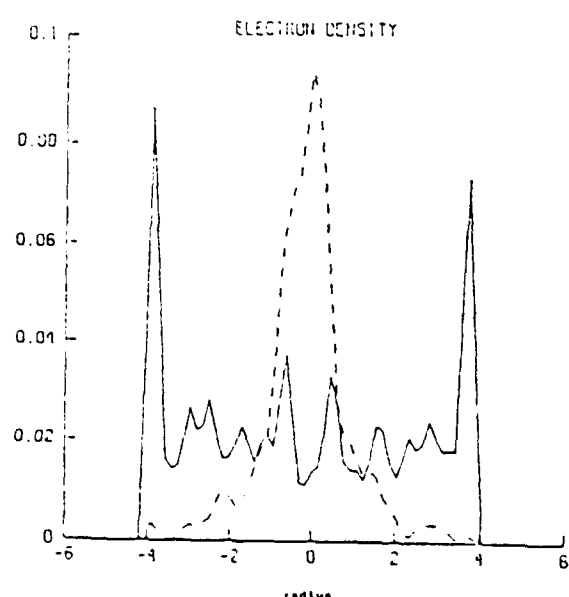


Fig. 2. Electron density vs. radius

In both figures, the dashed line is the density at  $t = 0$ , and the solid line is the density at  $t = 200$  ns.

#### CHANNEL STRENGTHENING

It is possible that the beam, itself, may be used to strengthen the channel during each of its passes around the racetrack. One strategy is to provide a neutral density high enough that the beam will ionize it to some extent generating an enhanced channel at each pass. Beam ionization would require neutral densities much higher than have been planned. If, for example, we allow the beam to ionize up to  $f = .2$ , the background density must be  $\sim 8$  microns. Another possibility, suggested by Sandia, is to shorten the length of the track so that the time between passes is about 25 ns so that channel will not have expanded significantly before the beam returns. In this case, the attraction of the negatively charged beam will reverse the expansion of the channel. We have done simulations for both cases, and in both cases, the channel ion density will be increased to provide space charge neutralization. However, in neither case will the channel guide the beam to the center of the transport vessel if the channel has drifted off center between passes.

Figures 3 and 4 show surface plots of the ion density as a function of time. In Fig. 3, there is no significant beam ionization, while in Fig. 4, the neutral gas density is high enough for the beam to generate a channel of strength  $f = .2$ .

ION CHANNEL DENSITY

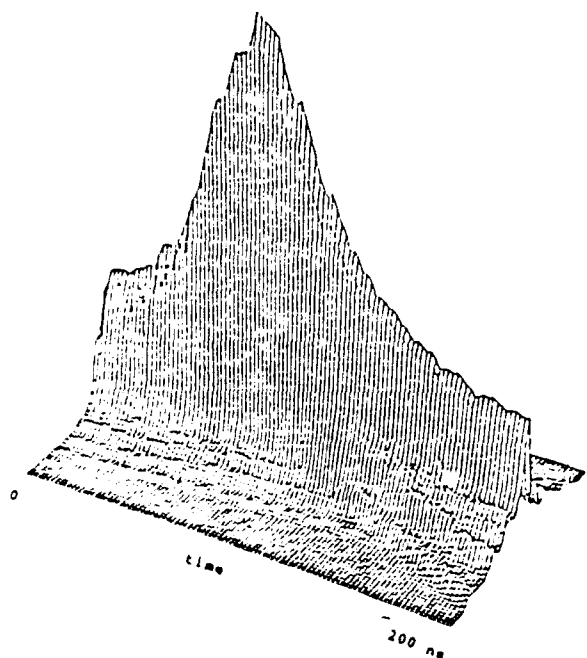


Figure 3.

ION CHANNEL DENSITY WITH BEAM GENERATED IONS

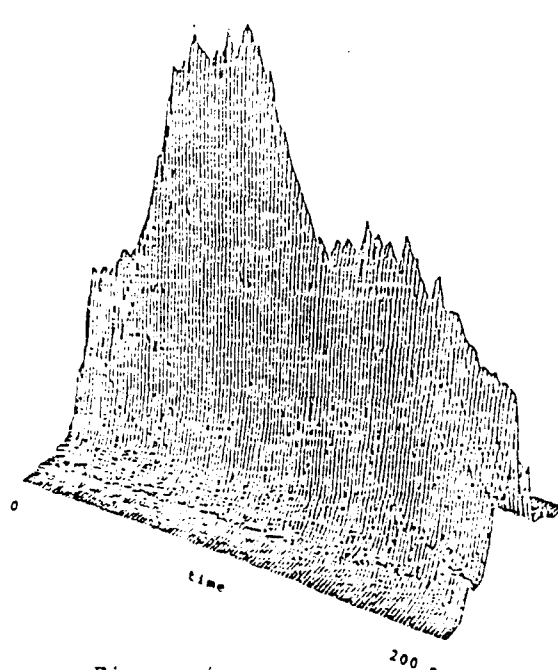


Figure 4.

### CHANNEL DRIFT

A major concern remains about the drifting of the channel centroid during the experiment. Although ion hose may not be a problem for beams whose length is ~ 25 ns, the beam and ion channel do interact. Simulations by John Wagner and Leon Feinstein have indicated that there is some channel drifting after the passage of the beam. There is no restoring force to center the channel in the beam line. In fact, if there is not a significant number of electrons, the electrostatic image forces due to the bare ion channel tend to accelerate it toward the wall. We can get an estimate of the time for the channel to hit the wall. The result is

$$c\tau = (I_A/2I_c m_i/m_e)^{1/2} b \ln\{(y_0/b + y(I_A/2I_c m_i/m_e)^{1/2}) - 1\}$$

where  $I_c = f I_b$

$I_A = 17$  kA

$b$  = wall radius

$y_0$  = initial offset

$y$  = initial velocity

An estimate of the time for our parameters is  $\tau \sim 350$  ns.

The consideration of channel motion will require more extensive investigation.

### CONCLUSIONS

Our analysis of ion channel motion in the Recirculating Linear Accelerator has shown that electrons from the chamber walls will not be effective in reducing the spread of the ion channel due to the electrostatic repulsion of the ions although there may be methods of replenishing the ions or reducing the spreading by using the beam itself. The problem of ion channel drift may be significant although more study will be necessary.

\*Work supported by the Defense Advanced Research Projects Agency, ARPA Order No. 4395, Amendment 80, monitored by Naval Surface Warfare Center.

# EROSION OF ELECTRON BEAMS IN THE RLA ACCELERATOR\*

R. F. Hubbard, G. Joyce and S. P. Slinker

Plasma Physics Division, Naval Research Laboratory, Washington, DC 20375

## I. INTRODUCTION

The Recirculating Linear Accelerator (RLA) currently being developed at Sandia National Laboratories will utilize ion-focused regime (IFR) transport in both straight and curved sections of the accelerator. In the curved sections, a vertical field approximately matched to the nominal beam energy and major radius of curvature of the bend will augment the IFR channel. In this paper, we describe ELBA simulation studies of beam transport and erosion in the RLA. The purposes of these studies are to determine beam head erosion rates for the RLA in both straight and curved sections, to estimate beam drifts in bends arising from such sources as local vertical field mismatch and hoop forces, to estimate emittance growth during transport and to study beam degradation in the broad, weak channels expected after the beam recirculates.

## II. METHODOLOGY

ELBA simulation code description: ELBA is a 3-D version of the FRIEZER axisymmetric particle simulation code. It is fully electromagnetic and solves the field equations in  $r$ ,  $\theta$ ,  $\zeta = ct - z$  and  $t$ . This doppler-shifted coordinate system is particularly well suited to treating IFR transport since it moves at the speed of light, making the coordinate  $\zeta$  an approximate constant of the motion for beam electrons. Although  $z$  is not a dynamical variable, diagnostics are usually transformed to the frozen ( $z$ ,  $\zeta$ ) coordinate system to facilitate comparison with experiments. The field solver in curved sections assumes a small aspect ratio  $r/R$  where  $r < a_w$  is the distance from the axis,  $a_w$  is the pipe radius and  $R$  is the major radius of the bend. ELBA employs an elegant mapping algorithm developed by Friedman<sup>1</sup> for treating beam dynamics in the bends. The implementation of this method in ELBA is described in more detail in Ref. 2. Beam and plasma electron dynamics are treated fully relativistically, and ion motion is neglected since we are concentrating on beam head effects. (Ion channel motion studies are reported elsewhere).<sup>3</sup> The

ratio of the bending field  $B_y$  to its matched value  $B_m = \beta\gamma_0 mc^2/eR$  can be specified arbitrarily.

Erosion Rate Diagnostics: In the RLA, the wall radius is not much larger than the beam radius  $a_b$ , so the full width half maximum (FWHM) of the beam current  $I_b(\zeta, z)$  is a convenient diagnostic for calculating the simulation erosion rate  $\beta_e$ . If  $\zeta_p(z)$  is defined by  $I(\zeta_p(z), z) = I_{max}/2$ , then  $\beta_e = (\zeta_p(z_2) - \zeta_p(z_1))/(z_2 - z_1) - a_w/R$ . The last term adjusts for slippage of the coordinate system in bends.<sup>2</sup> Results can be compared with the theoretical inductive erosion rate:  $\beta_e^{(th)} = fLv/\gamma$ . Here  $f$  is the ion-to-beam density ratio,  $v = I_b/(17 \text{ kA})$  and the inductance  $L = 2\ln(a_w/a_b)$ .

### III. SIMULATION RESULTS

Beam and channel parameters: A series of simulations were run with  $\gamma_0 = 10$ ,  $a_b = 1 \text{ cm}$ ,  $a_w = 4.5 \text{ cm}$ ,  $R = 84 \text{ cm}$ ,  $I_{max} = 10 \text{ kA}$  and channel radius  $a_{ch} = 1 \text{ cm}$ . A 128 cm long beam was transported 500 cm in straight or curved sections. The 500 cm in a curve corresponds to 340° although a single bend in the experiment is only 180°. Results from the various simulations are summarized in the table below.

Case	f	$B_y/B_m$	$\beta_e$	Transport Efficiency	$\zeta_r$	Comments
F1	0.5	N.A.	0.079	>0.99	5	Straight section, $\beta_e^{(th)}=0.079$
F2	0.5	1.0	0.119	>0.99	5	Curved; no sector magnet corr.
F3	0.5	1.0	0.110	>0.99	5	Curved; sector magnet on
F4	0.25	1.0	0.063	>0.99	5	Curved; lower f
F5	0.5	1.1	0.121	0.99	5	Curved; stronger vertical field
F6	0.25	1.1	0.063	0.99	5	Curved; lower f and higher $B_y$
F7	0.5	0.9	0.106	0.99	5	Curved; weaker vertical field
S1	0.25	1.0	0.041	0.96	60	Curved: std. moderate rise case
S2	0.25	N.A.	0.030	0.95	60	Straight; $\beta_e^{(th)} = 0.040$
S3	0.25	0.9	0.042	0.89	60	Curved; weaker vertical field
S4	0.25	1.1	0.059	0.96	60	Curved; stronger vertical field
W1 <sup>a</sup>	0.10	N.A.	0.010	0.84	60	Straight; $\beta_e^{(th)} = 0.008$
W2 <sup>a</sup>	0.10	1.0	0.013	0.84	60	Curved; std. weak channel case
W3 <sup>a</sup>	0.10	1.0	0.014	0.69	60	Curved; assumes 40% inc. in $\epsilon_n$
W4 <sup>a</sup>	0.10	1.0	0.030	0.48	60	Curved; $\gamma_0 = 10$
W6 <sup>a</sup>	0.10	0.9	0.022	0.29	60	Curved; weaker vertical field
W6 <sup>a</sup>	0.10	1.1	0.007	0.86	60	Curved; stronger vertical field

<sup>a</sup>Weak channel "recirculated" beam case:  $a_{ch} = 3.5 \text{ cm}$ ,  $\gamma_0 = 21$ : normalized emittance  $\epsilon_n$  matched for  $f=0.25$  and  $\gamma_0=10$  (as in previous cases).

Erosion results for fast rise cases: In order to facilitate comparison with analytical results, a series of simulations with a very short (5 cm) current rise length were carried out. For a channel-to-beam density ratio  $f = 0.5$  (Case F1), the erosion rate in a straight section simulation agreed with the analytical estimate  $\beta_e = 0.079$ . The rates in the curved section  $f = 0.5$  simulations (Cases F2, F3, F5 and F7) were typically 40% higher than in the straight case. As expected, the erosion rate dropped by almost a factor of two when  $f$  was reduced to 0.25 (Cases F4 and F6). Some cases included a 10% mismatch between the vertical field  $B_y$  and the matched value  $B_m$ .

Erosion and beam loss in moderate rise-rate cases: These cases (S1-S4) are similar to those above except that  $\zeta_r = 60$  cm. Erosion rates are somewhat lower than those produced in the previous cases. Figure 1 plots the displacements  $X(\zeta)$  and  $Y(\zeta)$  for a matched bending field simulation (Case S1). Ohmic energy loss cases the beam head to drift inward ( $X < 0$ ) while displacements in  $Y$  remain small. We believe that the small positive  $x$ -deflection in the beam body seen in Fig. 1 is due to the hoop force. Choosing  $B_y/B_m = 0.9$  instead of 1.0 (Case S3) results in a smaller inward drift in the beam head and a larger outward drift in the body.

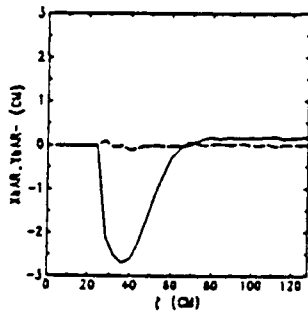


Fig 1. Beam displacement  $X(\zeta)$  (solid) and  $Y(\zeta)$  (dashed) at  $z=300$ cm: Case S1

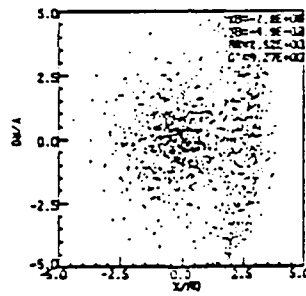


Fig 2. Pinched beam and escaping plasma electrons at  $z=318$ cm and  $\zeta=64$ cm: Case S1

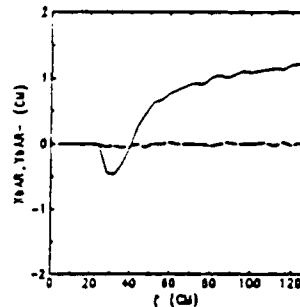


Fig 3. Beam displacement  $X(\zeta)$  and  $Y(z)$  at  $z=300$ cm for Case W2 (Weak ion channel;  $B_y=B_m$ ).  
y

Figure 2 plots the position of simulation particles at  $z = 318$  cm and  $\zeta = 64$  cm. Beam electrons are mostly confined to the area near the center, while the vertical "column" of particles consists of plasma electrons escaping along the vertical field lines.

Erosion and beam loss in a weak ion channel: Ion channel expansion between recirculations is a major concern for the racetrack design. Cases W1-

W6 mimic this effect by using a higher energy beam and a broader, weaker ion channel. As expected, these cases have substantially lower erosion rates but more particle loss to the wall. Particle loss is primarily due to evaporation and drifting; it is particularly severe in Cases W4 (low beam energy) and W5 (low vertical field). In addition, the ion channel is much less effective in centering the beam, as can be seen in the matched bending field case W2 in which the beam centroid is displaced by more than 1 cm (Fig. 3). This outward drift is due both to the hoop force and to a small increase on beam energy arising from inductive fields produced by rapid beam expansion just after the beam is injected.

There is very little growth in rms emittance even though the beam is not well matched to the channel strength. Particles which would normally contribute to emittance growth are generally lost to the wall instead. The results are consistent with end-to-end BUCKSHOT simulations by Wagner.<sup>4</sup>

#### IV. CONCLUSIONS AND REFERENCES

Simulations of the RLA using ELBA generally produce erosion rates  $\beta_e$  in the straight sections which agree with the standard inductive erosion formula. In curved sections  $\beta_e$  is generally 30-50% higher than in straight sections. A 10% mismatch in  $B_y$  cases a small shift in the beam centroid and has a modest effect on  $\beta_e$ . Weak channel ("recirculated") beam simulations show little erosion or emittance growth, but often exhibit large drifts from the axis and substantial current loss.

1. A. Friedman, D. Grote and I. Haber, Bull. Am. Phys. Soc. 34, 2064 (1989).
2. G. Joyce, et al., "ELBA - a Three-Dimensional Particle Simulation Code," these proceedings.
3. G. Joyce, et al., "IFR Propagation of Beams as Applied to RLA," these proceedings.
4. J. Wagner, "Simulations for RLA Experiment and Prototype," these proceedings.

\*Work supported by the Defense Advanced Research Projects Agency, ARPA Order No. 4395, Amendment No. 80, monitored by the Naval Surface Warfare Center.

ATOMIC AND PLASMA SURFACE INTERACTIONS  
IN ACCELERATORS AND IFR CELLS\*

by

A. W. ALI

Naval Research Laboratory, Washington, DC 20375

1. INTRODUCTION

DARPA is proceeding with its support and funding of new concepts in compact accelerators. Clearly the dominant issues for accelerators fall within the domain of pure plasma physics where electrons are moving in a vacuum, confined, guided, by magnetic fields and accelerated by electric fields. However, there is no such thing as a vacuum. Beam electrons are accelerated in chambers generally evacuated to some low pressures in the range of  $10^{-5}$  -  $10^{-9}$  Torr. Under these conditions, atmospheric species like N<sub>2</sub>, O<sub>2</sub> and contaminants as H<sub>2</sub>O, C and other gases are present, albeit in low densities in the range of  $10^7$  -  $10^{11}$  cm<sup>-3</sup>. These gaseous species will be ionized and dissociated by the circulating beam electrons resulting in a plasma (electrons and positive ions) which may impact the beam electrons, their trajectories, and their accelerations. However, there is another and very interesting phenomena which involves the inner surfaces of the accelerating chambers through which the beam electrons

\*This work was supported by Defense Advanced Research Project Agency under ARPA order No. 4395, Amendment No. 80 and monitored by the Naval Surface Weapon Center.

circulate. This phenomena is equally relevant to IFR cells which are often used in beam conditioning in electron beam propagation experiments. These surfaces act as a source of electrons, ions, and neutrals depending on various atomic processes which occur when particles and radiation fall on these surfaces. These surfaces generally acquire a monoatomic layer of atoms and molecules which are adsorbed into the surface. The adsorption occurs in time as a result of the gas flow in and out of the acceleration chambers and IFR cells (filling and evacuation) and by ions arriving at the surface. These ions acquire an electron and are neutralized. Hence, in a state of equilibrium one envisions a neutral species density distribution being maximum at the surface, decaying exponentially toward the center of the chamber. This gaseous distribution is what one calls the outgassing of the surfaces. Depending on the magnitude of the outgassing from the surface, considerable ionization can result by the interaction of the beam electrons with these species which are defusing into the chamber.

Additionally, ions accelerated by the beam will charge exchange with the neutrals generating fast neutrals which strike the chamber surface releasing additional atomic species into the chamber. Furthermore, the accelerated electrons will emit radiation which upon interaction with the surfaces generate additional electrons and ions. So will the accelerated plasma electrons. Accordingly, there is a host of atomic processes which occur in any accelerator chamber, IFR, and conditioning cells which must be considered and its impact on beam breakup and breakdown in IFR cells quantified.

## 2. BASIC ISSUES

The basic physical processes which lead to the enhancement of the ionization level in accelerators and IFR cells, change the

channel conductivity, and lead to the beam breakup, require detailed analysis. The physical processes are:

1. The beam electrons colliding with the ambient gas and the outgassed species resulting in the ionization of the neutral species, thus generating a plasma.
2. Accelerated plasma electrons and ions impacting the chamber surface, resulting in the ejection of atoms, negative ions, and molecules from species adsorbed to the surface. Such collisions contribute to adsorption, desorption or sputtering, reflection and surface heating. These processes, in general, increase the gas density near the surface and cause increased ionization by the collisions of charged particles with these species. The density of the adsorbed atoms or molecules generally is in the order of  $10^{15} \text{ cm}^{-3}$ , based on a monoatomic layer adsorbed on the surface. The gas density distribution starts from this value and decays exponentially to zero (in perfect vacuum) at the center of the accelerator and IFR chambers
3. Fast neutral species impacting the electrode surface. These fast neutrals generally arise as a result of charge exchange of accelerated ions with atoms or molecules, whereupon the fast ion becomes a fast neutral.

To determine the effects of these interactions on the beam stability, one may use analytic and ab-initio methods. The ab-inito approach, in general, is complicated and requires the time and space dependent simulations of electron and ion orbits in the accelerating chamber and their interactions with gas species and surfaces. This must be coupled to basic atomic processes in order to describe the ionization and the breakdown phenomenon. The simulation should be tailored to all appropriate accelerating chambers and IFR cells. In addition to detailed simulation method, simple analytic methods<sup>1</sup> can be utilized to obtain reasonable estimates for ionization rates and breakdown times for a wide range of electric fields, outgassed species densities, chamber diameter, beam circulation time and chamber radius, etc.

1. A. W. Ali, Laser and Particle Beams, 6, 105 (1988)

Distribution List\*

Naval Research Laboratory  
4555 Overlook Avenue, S.W.

Attn: CAPT J. J. Donegan, Jr. - Code 1000  
Dr. M. Lampe - Code 4792 (20 copies)  
Dr. T. Coffey - Code 1001  
Head, Office of Management & Admin - Code 1005  
Deputy Head, Office of Management & Admin - Code 1005.1  
Directives Staff, Office of Management & Admin - Code 1005.6  
Director of Technical Services - Code 2000  
ONR - Code 0124  
NRL Historian - Code 2604  
Dr. W. Ellis - Code 4000  
Dr. J. Boris - Code 4040  
Dr. M. Picone - Code 4040  
Dr. E. Oran - Code 4040  
Dr. M. Rosen - Code 4650  
Dr. M. Haftel - Code 4665  
Dr. S. Ossakow - Code 4700 (26 copies)  
Dr. V. Patel - Code 4701  
Dr. A. Robson - Code 4708  
Dr. M. Friedman - Code 4732  
Dr. R. Meger - Code 4750  
Dr. J. Antoniades - Code 4751  
Dr. T. Peyser - Code 4751  
Dr. D. Murphy - Code 4751  
Dr. R. Pechacek - Code 4750.1  
Dr. G. Cooperstein - Code 4770  
Dr. A. Ali - Code 4780  
Dr. D. Colombant - Code 4790  
Dr. R. Fernsler - Code 4790 (20 copies)  
Dr. I. Haber - Code 4790  
Dr. R. F. Hubbard - Code 4790 (20 copies)  
Dr. G. Joyce - Code 4790 (20 copies)  
Dr. Y. Lau - Code 4790  
Dr. S. P. Slinker - Code 4790 (20 copies)  
Dr. P. Sprangle - Code 4790  
Dr. C. M. Tang - 4790  
Dr. J. Krall - Code 4790  
B. Pitcher - Code 4790A  
Code 4790 (20 copies)  
Dr. S. Gold - Code 4793  
Dr. C. Kapetanakos - Code 4795  
Mr. P. Boris - SAIC (Code 5166)  
Library - Code 2628 (22 copies)  
D. Wilbanks - Code 2634  
Code 1220

\* Every name listed on distribution gets one copy except for those where extra copies are noted.

**Advanced Scientific Concepts, Inc.**  
2441 Foothill Lane  
Santa Barbara, CA 93105  
Attn: Dr. Roger Stettner

**Advanced Technologies Research**  
14900 Sweitzer Lane  
Laurel, MD 20707  
Attn: Mr. Daniel Weldman

**The Aerospace Corporation**  
Mail Stop M2-269  
P. O. Box 92957  
Los Angeles, CA 90009  
Attn: Dr. David L. McKenzie  
Dr. Carl J. Rice

**AFATL/DLJW**  
Elgin Force Base, FL 32542  
Attn: MAJ Louis W. Seller, Jr.

**Air Force Office of Scientific Research**  
Physical and Geophysical Sciences  
Bolling Air Force Base  
Washington, DC 20332  
Attn: Major Bruce Smith

**Air Force Weapons Laboratory**  
Kirtland Air Force Base  
Albuquerque, NM 87117-6008  
Attn: Dr. William L. Baker (AFWL/NTYP)  
Dr. Brendan B. Godfrey  
Dr. Inara Kuck

**Applied Physics Laboratory**  
The Johns Hopkins University  
Asst. to Dir. for Tech. Assessment  
Johns Hopkins Road  
Laurel, MD 20707  
Attn: Dr. Samuel Koslov

**Armed Forces Radiobiology**  
Research Institute  
Chief, MRAD  
NMC-NCR  
Bethesda, MD 20814-5145  
Attn: LCDR J. P. Jacobus

**U. S. Army Ballistics Research Laboratory**  
Aberdeen Proving Ground, Maryland 21005  
Attn: Dr. Donald Eccleshall (DRXBR-BM)  
Dr. Anand Prakash  
Dr. Clinton Hollandsworth

**Avco Everett Research Laboratory**  
2385 Revere Beach Pkwy  
Everett, Massachusetts 02149  
Attn: Dr. R. Patrick  
Dr. Dennis Reilly

**Ballena Systems Corporation**  
P. O. Box 752  
Alameda, CA 94501  
Attn: Dr. Adrian C. Smith  
Dr. William E. Wright

**Ballistic Missile Def. Ad. Tech. Ctr.**  
P.O. Box 1500  
Huntsville, Alabama 35807  
Attn: Dr. M. Hawie (BMDSATC-1)  
Dr. M. J. Lavan (BMDATC-E)  
Mr. Dan Whitener

**The Boeing Aerospace Company**  
MS-2E30  
Box 3999  
Seattle, WA 98124  
Attn: Dr. Robert C. Milnor

**Booz, Allen, and Hamilton**  
Crystal Square 2, Suite 1100  
1725 Jefferson Davis Highway  
Arlington, VA 22202-4136  
Attn: Dr. Charles M. Huddleston

**Brobeck and Associates**  
1235 10th Street  
Berkeley, CA 94710  
Attn: Dr. Francis C. Younger

**Chief of Naval Material**  
Office of Naval Technology  
MAT-0712, Room 503  
800 North Quincy Street  
Arlington, VA 22217  
Attn: Dr. Eli Zimet

**Commander**  
Space and Naval Warfare Systems Command  
National Center 1, Room 8E08  
Washington, DC 20363-5100  
Attn: RADM Robert L. Topping

**Cornell University**  
369 Upson Hall  
Ithaca, NY 14853  
Attn: Prof. David Hammer

Defense Advanced Research Projects Agency  
 1400 Wilson Blvd.  
 Arlington, VA 22209  
 Attn: Dr. H. L. Buchanan  
 Dr. B. Hui

Defense Nuclear Agency  
 Washington, DC 20305  
 Attn: Dr. Muhammad Owais (RAAE)  
 Dr. Michael Frankle  
 Dr. R. Gullickson

Department of Commerce  
 National Inst.of Standards and Tech.  
 Building 245, B-102  
 Washington, DC 20234  
 Attn: Dr. Mark A. D. Wilson  
 Dr. Steven M. Seltzer

Department of Energy  
 Washington, DC 20545  
 Attn: Dr. Wilmot Hess (ER20:GTN,  
 High Energy and Nuclear Physics)  
 Mr. Gerald J. Peters (G-256)

Department of the Navy  
 Chief of Naval Operations  
 The Pentagon  
 Washington, DC 20350  
 Attn: CAPT T. L. Sanders (OP981N3)  
 LCDR John Stanovich (OP981SDI)  
 LCDR Donald Melick (OP981SD)  
 Dr. Steve Bravy (OP981SDI)  
 Mr. Greg Montieth

Directed Technologies, Inc.  
 4001 Fairfax Drive, Suite 775  
 Arlington, VA 22203  
 Attn: Mr. Ira F. Kuhn  
 Dr. Nancy Chesser  
 Dr. Arthur Lee  
 Ms. Marla Shain

Directed Technologies, Inc.  
 5945 Pacific Center Blvd.  
 Suite 510  
 San Diego, CA 92121  
 Attn: Dr. Robert A. Jacobsen

Dr. Harald O. Dogliani  
 P. O. Box 503  
 Los Alamos, NM 87544

C. S. Draper Laboratories  
 555 Technology Square  
 Cambridge, Massachusetts 02139  
 Attn: Dr. E. Olsson

ESL, Inc.  
 Mail Stop M-4216  
 495 Jova Drive  
 Sunnyvale, CA 94088  
 Attn: Dr. Robert A. Marth

FM Technologies, Inc.  
 10529B Braddock Road  
 Fairfax, VA 22032  
 Attn: Dr. F. M. Mako

GA Technologies, Inc.  
 P. O. Box 85608  
 Code 02/503  
 San Diego, CA 93138  
 Attn: Dr. Vincent Chen  
 Dr. Hiroyuki Ikez

General Dynamics Corporation  
 1745 Jefferson Davis Highway  
 Suite 1000  
 Arlington, VA 22202  
 Attn: Dr. Daniel W. Roth

General Dynamics Corporation  
 Pomona Division  
 1675 W. Mission Blvd.  
 P. O. Box 2507  
 Pomona, CA 92769-2507  
 Attn: Dr. Ken W. Hawko  
 Mr. C. L. Featherstone

Grumman Corporation  
 Grumman Aerospace Research Ctr.  
 Bethpage, NY 11714-3580  
 Attn: Dr. Richard G. Madonna

Headquarters, Department of Army  
 DAMOFDE, Room 2D547  
 The Pentagon  
 Washington, DC 20310-0460  
 Attn: LTCOL Lou Goldberg

HQ Foreign Technology Division  
 Wright-Patterson AFB, OH 45433  
 Attn: TUTD/Dr. C. Joseph Butler

HQ USAF/TXN  
 Patrick Air Force Base, FL 32925  
 Attn: CAPT Joseph Nicholas

**Hudson Institute**  
Center for Naval Analyses  
Alexandria, VA 22302  
Attn: Dr. F. Bomse

**Hy-Tech Research Corp.**  
P. O. Box 3422 FSS  
Radford, VA 24143  
Attn: Dr. Edward Yadlowsky

**Idaho Engineering National Lab.**  
P. O. Box 1625  
Idaho Falls, ID 83415  
Attn: Dr. Francis Tsang

**Institute for Defense Analyses**  
1801 N. Beauregard Street  
Alexandria, VA 22311  
Attn: Dr. Deborah Levin  
Ms. M. Smith

**IRT Corporation**  
3030 Callan Road  
San Diego, CA 92121  
Attn: Dr. David Phelps

**JAYCOR**  
11011 Torreyana Road  
P. O. Box 85154  
San Diego, CA 92138-9259  
Attn: Dr. Franklin S. Felber  
Dr. Seung Kai Wong

**JAYCOR**  
39650 Libery Street, Suite 320  
Freemont, CA 94538  
Attn: Dr. Kendal Casey

**Joint Institute for Laboratory  
Astrophysics**  
National Bureau of Standards and  
University of Colorado  
Boulder, CO 80309  
Attn: Dr. Arthur V. Phelps

**Kaman Sciences**  
P. O. Drawer QQ  
Santa Barbara, CA 93102  
Attn: Dr. W. Hobbs

**La Jolla Institute**  
P. O. Box 1434  
La Jolla, CA 92038  
Attn: Dr. K. Brueckner

**Lawrence Berkeley Laboratory**  
University of California  
Berkeley, CA 94720  
Attn: Dr. Edward P. Lee  
Dr. Thomas Fessenden  
Dr. William Fawley  
Dr. Roger Bangert

**Lawrence Livermore National Laboratory**  
University of California  
Livermore, California 94550  
Attn: Mr. Arthur G. Cole  
Dr. Michael Delong  
MAJ Kenneth Dreyer  
Dr. Ed Farley  
Dr. Alex Glass  
Dr. George Craig  
Dr. C. V. Johnson, III  
Dr. George Kamin  
Dr. V. Kelvin Neil  
Dr. Arthur C. Paul  
Mr. Louis Reginato  
Mr. Doyle Rogers  
Dr. Dennis R. Slaughter  
Dr. David Whittum  
Dr. Simon S. Yu  
Dr. Frank Chambers  
Dr. James W.-K. Mark, L-477  
Dr. William Barletta  
Dr. William Sharp  
Dr. John K. Boyd  
Dr. John Clark  
Dr. George J. Caporaso  
Dr. Donald Prosnitz  
Dr. John Stewart  
Dr. Y. P. Chong  
Dr. Hans Kruger  
Dr. Thaddeus J. Orzechowski  
Dr. John T. Weir  
Dr. Yu-Jiuan Chen

Dr. James E. Leiss  
13013 Chestnut Oak Drive  
Gaithersburg, MD 20878

**Lockheed Missiles and Space Co.**  
3251 Hanover St.  
Bldg. 205, Dept 92-20  
Palo Alto, CA 94304  
Attn: Dr. John Siambis

Los Alamos National Laboratory  
P.O. Box 1663  
Los Alamos, NM 87545

Attn: Dr. L. Thode  
Dr. H. Dogliani, MS-5000  
Mr. R. Carlson, MS-P940  
Dr. Carl Ekdahl, MS-D410  
Dr. Joseph Mack  
Dr. Melvin I. Buchwald  
Dr. David C. Moir  
Dr. Daniel S. Prono  
Dr. S. Czuchlewski  
Dr. Thomas P. Starke  
Dr. Donald D. Cobb, D466  
Dr. Robert R. Karl, D466  
Dr. William B. Maier  
Dr. John P. Rink  
Dr. David Chamberlin

Maxwell Laboratories Inc.  
8888 Balboa Avenue  
San Diego, CA 92123  
Attn: Dr. Ken Whitham  
Dr. S. Echouse

McDonnell Douglas Research Laboratories  
Dept. 223, Bldg. 33, Level 45  
Box 516  
St. Louis, MO 63166  
Attn: Dr. Carl Leader  
Dr. Frank Bieniosek  
Dr. John Honig

Mission Research Corporation  
1720 Randolph Road, S.E.  
Albuquerque, NM 87106  
Attn: Dr. Thomas Hughes  
Dr. Lawrence Wright  
Dr. Kenneth Struve  
Dr. Michael Mostrom  
Dr. Dale Welch

Mission Research Corporation  
P. O. Drawer 719  
Santa Barbara, California 93102  
Attn: Dr. C. Longmire  
Dr. N. Carron

Mission Research Corporation  
8560 Cinderbed Road  
Suite 700  
Newington, VA 22122  
Attn: Dr. Khanh Nguyen

National Inst. of Standards & Tech.  
Gaithersburg, Maryland 20760  
Attn: Dr. Mark Wilson

National Inst. of Standards & Tech.  
Radiation Physics Bldg. Room C229  
Washington, DC 20234  
Attn: Dr. Wayne Cassatt

National Security Agency  
4928 College Avenue  
College Park, MD 20740  
Attn: Dr. Albert J. Leyendecker

Naval Ocean Systems Center  
San Diego, CA 92152  
Attn: CAPT James Fontana  
Mrs. Teresita Finch  
Dr. Rodney Buntzen

Naval Postgraduate School  
Physics Department (Code 61)  
Monterey, CA 93940  
Attn: Prof. John R. Neighbours  
Prof. Fred Buskirk  
Prof. Kai Woehler  
Prof. Xavier Maruyama

Naval Surface Warfare Center  
Dahlgren, VA 22448-5000  
Attn: Dr. E. M. Williams  
Mr. C. E. Gallaher  
Mr. Lawrence Luessen  
Ms. Theresa Houghton  
Dr. Ronald J. Gripshover  
Dr. S. L. Moran  
Dr. Edwin Ball

Naval Surface Warfare Center  
White Oak Laboratory  
Code R-41  
Silver Spring, Maryland 20903-5000  
Attn: CAPT R. P. Fuscaldo  
Dr. Thomas A. Clare  
CAPT R. W. Moore  
Dr. Ira Blatstein  
Mr. Kenneth Caudle  
Mr. Carl Larson  
Dr. Robert DeWitt  
Dr. Ralph Schneider  
Dr. Joel Miller  
Dr. Stanley Stern  
Dr. Omer Goktepe  
Dr. A. L. Licht  
Dr. Joon Choe  
Mr. David Demske  
Dr. Jag Sharma  
Mr. W. M. Hinckley  
Dr. H. S. Uhm  
Dr. R. Fiorito  
Dr. R. Stark  
Dr. H. C. Chen  
Dr. D. Rule  
Dr. Matt Brown  
Mrs. Carolyn Fisher (G42)  
Dr. Eugene E. Nolting (H23)

Naval Technical Intelligence Center  
Code DA52  
4301 Suitland Road  
Washington, DC 20395  
Attn: Mr. Mark Chapman

New Mexico State University  
Research Center  
Box RC  
Las Cruces, NM 88003-0001  
Attn: Dr. Leon J. Radziemski

Northeastern University  
Dept. of Elec. Engineering  
360 Huntington Avenue  
Boston, MA 02115  
Attn: Dr. Philip Serafim

North Star Research Corp.  
555 Zuni, S. E.  
Albuquerque, NM 87104  
Attn: Dr. Richard Adler

Oak Ridge National Laboratory  
Health & Safety Research Div.  
P. O. Box X  
Oak Ridge, TN 37830  
Attn: Dr. Rufus H. Ritchie  
Dr. O. Crawford

Office of the Chief of Naval Operation  
Strategic and Theatre Nuclear Warfare  
OP-654E4  
The Pentagon  
Washington, DC 20350  
Attn: Dr. Yong S. Park

Office of Naval Research  
800 North Quincy Street  
Arlington, VA 22217  
Attn: Dr. C. W. Roberson  
Dr. F. Saalfeld

Office of Naval Research (2 copies)  
Department of the Navy  
Code 01231C  
Arlington, VA 22217

Office of Under Secretary of Defense  
Research and Engineering  
Room 3E1034  
The Pentagon  
Washington, DC 20301  
Attn: Dr. John MacCallum

OSWR  
P. O. Box 1925  
Washington, DC 20013  
Attn: Dr. Jose F. Pina

PhotoMetrics, Inc.  
4 Arrow Drive  
Woburn, MA 01801  
Attn: Dr. Irving Kofsky

Physics International, Inc.  
2700 Merced Street  
San Leandro, CA. 94577  
Attn: Dr. E. Goldman  
Dr. James Benford  
Dr. George B. Frazier  
Mr. Ralph Genuario

Princeton University  
Plasma Physics Laboratory  
Princeton, NJ 08540  
Attn: Dr. Francis Perkins, Jr.

Pulse Sciences, Inc.  
600 McCormack Street  
San Leandro, CA 94577  
Attn: Dr. Sidney Putnam  
Dr. Vernon Bailey  
Dr. M. Tiefenbach  
Dr. J. Edighoffer  
Mr. James Fockler

Pulse Sciences, Inc.  
2001 Wilshire Boulevard  
Suite 600  
Santa Monica, CA 90403  
Attn: Dr. John R. Bayless

R&D Associates  
301A South West Street  
Alexandria, VA 22314  
Attn: Mr. Ihor Vitkovitsky  
Dr. Peter Turchi

The Rand Corporation  
2100 M Street, NW  
Washington, DC 20037  
Attn: Dr. Nikita Wells  
Mr. Simon Kassel

Sandia National Laboratory  
Albuquerque, NM 87115  
Attn: Dr. Collins Clark  
Dr. John Freeman/1241  
Dr. Charles Frost  
Dr. Gerald N. Hays  
Dr. Michael G. Mazarakis/1272  
Dr. John Wagner/1241  
Dr. Ron Lipinski/1274  
Dr. James Poukey  
Dr. Milton J. Clauser/1261  
Dr. Kenneth R. Prestwich/1240  
Dr. Kevin O'Brien  
Dr. Isaac R. Shokair  
Dr. J. Pace VanDevender/1200  
Dr. J. T. Crow  
Dr. S. Shope  
Dr. B. N. Turman  
Dr. C. Olson  
Dr. Richard Adams  
Dr. Malcolm Buttram  
Mr. Charle Crist  
Dr. Susan Fisher  
Dr. John Keizur  
Dr. Gordon T. Leifeste  
Dr. Raymond W. Lemke  
Dr. Juan Ramirez  
Dr. James Rice  
Dr. Michael Wilson

Science Applications Intl. Corp.  
2109 Air Park Road, S. E.  
Albuquerque, NM 87106  
Attn: Dr. R. Richardson  
Dr. Michael D. Haworth  
Dr. Alan J. Toepfer

Science Applications Intl. Corp.  
5150 El Camino Road  
Los Altos, CA 94022  
Attn: Dr. R. R. Johnston  
Dr. Leon Feinstein  
Dr. Douglas Keeley  
Dr. E. Roland Parkinson

Science Applications Intl. Corp.  
1710 Goodridge Drive  
McLean, VA 22102  
Attn: Mr. W. Chadsey  
Dr. A Drobot  
Dr. K. Papadopoulos  
Dr. William W. Rienstra  
Dr. Alfred Mondelli  
Dr. D. Chernin  
Dr. R. Tsang  
Dr. J. Petillo  
Dr. G. Bourianoff  
Ms. K. Wilson

Science Research Laboratory, Inc.  
1600 Wilson Boulevard  
Suite 1200  
Arlington, VA 22209  
Attn: Dr. Joseph Mangano  
Dr. Daniel Birx

Commander  
Space & Naval Warfare Systems Command  
PMW-145  
Washington, DC 20363-5100  
Attn: CDR W. Fritchie  
Mr. D. Merritt

Space Power Institute  
315 Leach Science Center  
Auburn University  
Auburn, AL 36845-3501  
Attn: Prof. M. Frank Rose

Spectra Technology  
2755 Northup Way  
Bellevue, WA 98004  
Attn: Dr. Dennis Loventhal  
Dr. Steve Baughman  
Dr. James Ewing

SRI International  
PSO-15  
Molecular Physics Laboratory  
333 Ravenswood Avenue  
Menlo Park, CA 94025  
Attn: Dr. Donald Eckstrom  
Dr. Kenneth R. Stalder  
Dr. Roberta Saxon  
Dr. Jay Dickerson

Strategic Defense Initiative Org.  
SDIO/T/DEO  
The Pentagon  
Washington, DC 20301-7100  
Attn: COL Thomas Meyer (DEWO)  
LTC Michael Toole (DEWO)  
MAJ J. Wills  
Dr. Dwight Duston  
LTC Ed Pogue  
Dr. Kevin Probst  
Dr. Charles Sharn

System Planning Corporation  
1500 Wilson Boulevard, Room 1213W  
Arlington, VA 22209  
Attn: Mr. James T. Lacatski

Titan/Spectron, Inc.  
P. O. Box 4399  
Albuquerque, NM 87196  
Attn: Dr. R. Bruce Miller  
Dr. John Smith

Titan Systems, Inc.  
5910 Pacific Center Blvd.  
San Diego, CA 92121  
Attn: Dr. R. M. Dove, Jr.

Tetra Corporation  
4905 Hawkins Street, N. E.  
Albuquerque, NM 87109-4345  
Attn: Mr. William Money

University of California  
Physics Department  
Irvine, CA 92664  
Attn: Dr. Gregory Benford  
Dr. Norman Rostoker

University of California  
San Diego, CA 92110  
Attn: Dr. Marshall N. Rosenbluth

UCLA  
Physics Department  
Los Angeles, CA 90024  
Attn: Dr. F. Chen  
Dr. C. Joshi  
Dr. J. Dawson  
Dr. N. Luhmann  
Dr. W. Barletta  
Dr. T. Katsouleas

University of Colorado  
Dept. of Astrophysical, Planetary  
& Atmospheric Sciences  
Boulder, CO 80309  
Attn: Dr. Scott Robertson

University of Illinois at Chicago  
Dept. of Physics  
P. O. Box 4348  
Chicago, IL 60680  
Attn: Dr. Charles K. Rhodes

University of Maryland  
College Park, MD 20742  
Attn: Dr. J. Goldhar  
Dr. W. Destler  
Dr. C. Striffler  
Dr. Moon-Jhong Rhee

University of Michigan  
Dept. of Nuclear Engineering  
Ann Arbor, MI 48109  
Attn: Prof. Terry Kammash  
Prof. R. Gilgenbach

University of New Mexico  
Dept. of Chem. & Nuclear Engineering  
Albuquerque, NM 87131  
Attn: Prof. Stanley Humphries

Commander  
U. S. Army Laboratory Command  
2800 Powder Mill Road  
Adelphi, MD 20783-1145  
Attn: George Albrecht (AMSLC-TP-PL)

U. S. Army Combined Army Center  
ATZL-CAG  
Ft. Leavenworth, KS 68027-5000  
Attn: LTC Orville Stokes

Yale University  
Mason Laboratory  
New Haven, CN 06520  
Attn: Dr. Ira Bernstein

Director of Research  
U.S. Naval Academy  
Annapolis, MD 21402 (2 copies)